

Data-driven dimensional analysis of heat transfer in irradiated particle-laden turbulent flow

Lluís Jofre^{a,b,*}, Zachary R. del Rosario^c, Gianluca Iaccarino^{a,d}

^aCenter for Turbulence Research, Stanford University, Stanford, CA 94305, USA

^bDepartment of Fluid Mechanics, Technical University of Catalonia - BarcelonaTech, Spain

^cDepartment of Aeronautics and Astronautics, Stanford University, Stanford, CA 94305, USA

^dInstitute for Computational and Mathematical Engineering, Stanford University, Stanford, CA 94305, USA

Abstract

The study of thermal radiation interacting with particle-laden turbulence is of great importance in a wide range of scientific and engineering applications. The fundamental and applied study of such systems is challenging as a result of the large number of thermo-fluid mechanisms governing the underlying physics. This complexity is significantly reduced by transforming the problem of interest into its scale-free form by means of dimensional analysis techniques. However, the theoretical framework of classical dimensional analysis presents the limitations of not providing a unique set of dimensionless groups, and no support for measuring the relative importance between them. In the interest of addressing these shortfalls for multiphysics turbulent flow applications, we present a semi-empirical dimensional analysis approach to efficiently extract important dimensionless groups from data obtained by means of computational (or laboratory) experiments. The methodology presented is then used to characterize important dimensionless groups in irradiated particle-laden turbulence. The study concludes that two dimensionless groups are responsible for most of the variation in the system's thermal response, with the absorption of radiation by particles, the radiative energy deposition rate and the turbulent flow mixing the most important thermo-fluid mechanisms. The generality of the results obtained can be leveraged to effectively reduce the dimensionality of irradiated particle-laden turbulent flows in research studies and in the design and optimization of similar systems.

Keywords: Active subspaces; Data science; Dimension reduction; Particle-laden flow; Radiative heat transfer; Turbulence

1. Introduction

The analysis, design and optimization of multiphysics turbulent flow phenomena generally involves the understanding and characterization of a large variety of physics mechanisms. The inherent challenge of operating with such complex systems is typically reduced by transforming the problem of interest into its dimensionless form. Dimensional analysis provides a compelling framework to perform the operations required, as well as support for analyzing the resulting scale-free system. Its underlying principle is based on the notion of similarity, which postulates that relationships between physical quantities do not vary if the measurement units are changed. This central result implies that simpler small-scale experiments can be utilized to study larger-scale phenomena. In addition, one major advantage is that dimensional analysis typically yields a smaller number of independent dimensionless variables than the original measured quantities. Hence, the dimensionality of the system is reduced, and as a result fewer (potentially expensive) experiments are needed to characterize its response, i.e., quantity of interest (QoI), to a set of inputs.

*Corresponding Author

Email addresses: jofre@stanford.edu (Lluís Jofre), zdr@stanford.edu (Zachary R. del Rosario), jops@stanford.edu (Gianluca Iaccarino)

1.1. Irradiated particle-laden turbulence

Turbulent flow laden with inertial particles exposed to thermal radiation is encountered in a wide range of natural phenomena and industrial applications. For instance, it is well established that turbulence-driven particle inhomogeneities play a fundamental role in determining the rate of droplet coalescence and evaporation in ocean sprays [1] and atmospheric clouds [2]. This problem is also important in fires due to the strong interaction between turbulence, soot particles, and radiation that result in complex heat transfer mechanisms [3]. From an industrial viewpoint, important applications include the atomization of liquid fuels in combustion chambers [4, 5], soot formation in rocket engines [6], and more recently, volumetric particle-based receivers for energy harvesting [7] in concentrated solar power (CSP) systems.

Even in the most elementary configuration, i.e., homogeneous isotropic turbulence (HIT), particle-laden turbulent flow is known to exhibit complex interactions between the carrier and dispersed phases in the form of preferential concentration and turbulence modulation [8]. Preferential concentration is the mechanism by which heavy particles tend to avoid intense vortical motions and accumulate in regions of high strain rate, whereas turbulence modulation refers to the alteration of fluid flow characteristics in the near-field region of particle clusters as a result of two-way coupling effects, e.g., enhanced dissipation, kinetic energy transfer, or formation of wakes. The physical complexity is further increased by the simple addition of solid walls as turbophoresis [9], i.e., tendency of particles to migrate towards regions of decreasing turbulence levels, becomes an important mechanism for augmenting the inhomogeneity in the spatial distribution of the dispersed phase by driving particle accumulation at the walls.

Consequently, the analysis and characterization of particle-laden turbulent flow are challenging endeavors, and therefore many experimental and computational research studies have been devoted to this objective over the past decades, e.g., [9, 10, 11, 12, 13, 14]. In addition to particle-flow coupling, the problem studied in this work involves an additional layer of complexity by considering the heat transfer from the particles to the fluid via radiation absorption. The engineering application motivating the understanding of these phenomena is the improvement of energy harvesting in volumetric particle-based solar receivers. This innovative technology is expected to increase the performance of CSP plants by avoiding the necessity of heat-exchanging stages. However, the physical mechanisms governing irradiated particle-laden turbulent flow are still not fully comprehended, and consequently under intense active research. For example, Zamansky et al. [15] studied the interaction between radiation, particles, and buoyancy in HIT by means of point-particle direct numerical simulations under the assumption of uniform radiation intensity in an optically thin environment. The study revealed how non-uniformities of the gas-particle mixture resulted in inhomogeneities in heat absorption, and therefore in spatial temperature variations that induced large-scale fluid motion by local gas expansion and buoyancy. The resulting baroclinic vorticity production triggered a feedback loop that generated larger non-uniformities by centrifuging the inertial particles leading to new non-uniformities in heat absorption. In the context of buoyancy effects in HIT, Frankel et al. [16] investigated the impact of heating on the settling of particles, finding that, contrary to non-heated particles which enhance small- and large-scale turbulent motions when their settling velocity is sufficiently high compared to the Kolmogorov velocity, the heating of particles resulted in a significant reduction of the mean settling velocity caused by rising buoyant plumes in the vicinity of particle clusters and which affected all scales of turbulence. However, in regimes relevant to particle-based solar receivers, the background turbulence dominates over the buoyancy effects as the Froude number of the systems are typically very large. This problem was studied by Pouransari & Mani [17] by considering a convective flow of gas and particles subject to radiation and in the limit of negligible buoyancy effects. In their study, it is shown how different particle concentration patterns, resulting from different Stokes numbers, provide different heat transfer rates between particles and gas. A similar flow configuration, but considering polydispersity of particles, has been recently analyzed by Rahmani et al. [18], finding also that the effective heat transfer rate between the two phases is impacted by particle clustering in addition to polydispersity.

1.2. Physical basis of dimensional analysis

Dimensional analysis offers a general framework for reducing complex physical systems to a simpler form prior to obtaining a quantitative answer. Central to its basis is the concept of similarity [19]. In physical

63 terms, similarity refers to some equivalence between two phenomena that are quantitatively different. In
64 mathematical form, similarity refers to a transformation that preserves some property, implying that a
65 smaller number of variables is needed to explain the phenomenon at hand. For example, under particular
66 conditions and simplifications, there is a direct relationship between the movement of large masses of air
67 in the atmosphere and the motion of a fluid in a small-scale laboratory (or computational) model. The
68 challenges are to find (i) those conditions and (ii) the transformation between them; in this case, the same
69 ratio of inertial to viscous forces, i.e., Reynolds number. Dimensional analysis aims to help solve these
70 two challenges in general problems by providing a set of mathematical techniques and methodologies. Its
71 main utility derives from its ability to contract, or make more evident, the functional form of physical
72 relationships.

73 In problems for which a set of equations can be formulated to describe the governing physics, similar-
74 ity can be inferred by normalizing all the equations and boundary conditions in terms of quantities that
75 characterize the problem, to subsequently identify the dimensionless groups that appear in the resulting
76 dimensionless equations. This is an inspectional form of similarity analysis [20]. Since inspectional analysis
77 takes advantage of the problem's complete mathematical description, it typically reveals a higher degree of
78 similarity than a blind, less informed, dimensional analysis, and therefore provides more powerful insight.

79 Although some of the basic ideas had already been proposed by Fourier in the first quarter of the
80 nineteenth century, the foundations of similarity and dimensional analysis were mainly developed toward
81 the end of that century by the seminal works, among others, of Lord Rayleigh, Reynolds, Maxwell and
82 Froude [21]. During the first quarter of the following century, the principles of the discipline were mature
83 and essentially in place due to the appearance of Buckingham's π theorem [22], and the publication of
84 Bridgman's monograph [23], which still remains the classic reference in the field. Since then, the litera-
85 ture has grown extraordinarily. Present scientific and engineering applications include aerodynamics [24],
86 propulsion and combustion [25], radiation [26], astrophysics [27], impact dynamics [28], chemical reactions
87 and processing [29], biology [30], and even economics [31].

88 The premise of dimensional analysis is that the form of any physics-based description of a system,
89 e.g., conservation equations and experimental correlations, must be such that the relationship between the
90 actual physical quantities remains valid independently of the magnitudes of the base units utilized. This
91 feature provides a number of very useful outcomes in terms of (i) facilitating the inference of similarity
92 laws, (ii) producing a basis for out-of-scale modeling, (iii) providing support for dimensionality reduction
93 approaches, and (iv) obtaining insight that is independent of the system of units utilized. However, as any
94 other scientific discipline, it presents some limitations. For example, (i) an incomplete, or unnecessary, set
95 of independent variables may significantly complicate the analysis [32], (ii) the framework is not robust to
96 external simplifying assumptions, (iii) the set of scale-free relations obtained is not unique, and (iv) there
97 is no formal approach for quantifying the relative importance between dimensionless groups. In this regard,
98 this work proposes a data-driven methodology inspired by the work of Constantine et al. [33], and aimed at
99 addressing the last two shortfalls by means of augmenting Buckingham's π theorem with ideas developed
100 in the fields of ridge functions [34, 35] and active subspaces [36]. In addition, the methodology presented is
101 supplemented (i) with a novel diagnostic tool (principal angles) for use when estimating active subspaces,
102 and (ii) the physical interpretability of the results is enhanced by introducing a linear algebra approach to
103 re-express the dimensionless groups on a user-selected basis that can be combined with inspectional analysis.

104 *1.3. Objectives and organization of the work*

105 As previously introduced, the exploration and analysis of complex systems, especially multiphysics flow
106 problems, can be systematically approached by considering the important dimensionless groups character-
107 izing the relations between the underlying physics phenomena. Extraction of the dimensionless parameters
108 is also very useful for engineering practice as it allows one to identify important directions in the input
109 space for the efficient design and optimization of systems. Therefore, the objectives of this work are (i) to
110 present a semi-empirical methodology, based on the seminal work by Constantine et al. [33], to effectively
111 infer important dimensionless groups from data obtained by means of computational (or laboratory) flow
112 experiments, and (ii) to utilize the methodology developed to characterize important dimensionless groups
113 in irradiated particle-laden turbulence.

114 The paper is organized as follows. In Section 2, the physics modeling and computational approach
 115 utilized to study irradiated particle-laden turbulence are described. A detailed presentation of the data-
 116 driven dimensional analysis methodology is given in Section 3. In Section 4, the configuration of the model
 117 problem is described in terms of physics, setup, and system parameters. Next, in Section 5, results and their
 118 analysis are discussed. Finally, in Section 6, the work is concluded and future directions are proposed.

119 2. Modeling of irradiated particle-laden turbulence

120 The physics modeling of dispersed multiphase flow can be separated into two main formulations based
 121 on the strategy chosen to describe the particles (dispersed) and fluid (carrier) phases: Eulerian-Eulerian
 122 (EE) and Lagrangian-Eulerian (LE). The EE type is a random field approach in which both dispersed and
 123 carrier phases are represented as random fields in the Eulerian frame, whereas the LE class is a point-based
 124 formulation in which the dispersed phase is represented as a stochastic process in a Lagrangian setting
 125 and the carrier phase is represented as a random field in the Eulerian frame. The scope of this work is
 126 restricted to LE schemes as some of its properties are advantageous for the application of interest, e.g.,
 127 applicability to a wide range of particle loadings and sizes. The LE approach can be further decomposed
 128 into different subcategories — see the review by Subramaniam [37] for a detailed exposition — corresponding
 129 to: (i) direct numerical simulation (DNS) with fully-resolved particles, (ii) point particle (PP) DNS with
 130 physical particles, (iii) PP-DNS with stochastic (parcel) particles, (iv) large-eddy simulation (LES) with
 131 physical or stochastic particles, and (v) Reynolds-averaged Navier-Stokes (RANS) approaches.

132 2.1. Point particle direct numerical simulation

133 Within the realm of LE formulations, DNS with fully-resolved particles is the modeling approach with
 134 highest fluid dynamics fidelity as the relevant flow structures in the bulk of the fluid, i.e., integral to Kol-
 135 mogorov turbulent scales, and near the particles, e.g., boundary layers and wakes, are resolved. However,
 136 this extreme level of resolution comes at the cost of exceedingly large computing resources, and therefore
 137 simulations are restricted typically to hundreds/thousands of particles. In the case of particle sizes being
 138 smaller than the smallest flow scales, an efficient alternative is to represent them as infinitesimally small
 139 Lagrangian points, i.e., PP-DNS, with masses m_p and time-dependent positions \mathbf{x}_p and velocities \mathbf{v}_p . This
 140 mesoscopic description of particles significantly reduces the computational cost of simulating dispersed multi-
 141 phase flow, but requires assumed models to represent inter-phase transfer terms such as particle acceleration
 142 and fluid-particle heat exchange. The conservation equations describing irradiated, dispersed multiphase
 143 flow following a PP-DNS representation are introduced in the subsections below.

144 2.1.1. Eulerian description of turbulent flow

For the thermodynamic regimes studied in this work, the carrier fluid is well approximated by the ideal-
 gas equation of state (EoS) $P_{th} = \rho_f R_f T_f$, where P_{th} is the thermodynamic pressure, ρ_f is the fluid density,
 $R_f = C_{P,f} - C_{v,f}$ is the specific gas constant of the fluid with $C_{P,f}$ and $C_{v,f}$ the isobaric and isochoric
 specific heat capacities, respectively, and T_f is the fluid temperature. As indicated by the EoS, density
 varies with temperature and pressure. However, the Mach number of the flow — $Ma = u/c$ with u the local
 flow velocity and c the speed of sound of the medium — is small for the range of conditions considered, i.e.,
 $Ma \ll 1$. As a result, the low-Mach-number approximation is utilized to separate the hydrodynamic part,
 $p \ll P_{th}$, from the total pressure, $P(\mathbf{x}, t) = P_{th}(t) + p(\mathbf{x}, t)$. This decomposition results in the following
 equations of fluid motion

$$\frac{\partial \rho_f}{\partial t} + \nabla \cdot (\rho_f \mathbf{u}_f) = 0, \quad (1)$$

$$\frac{\partial (\rho_f \mathbf{u}_f)}{\partial t} + \nabla \cdot (\rho_f \mathbf{u}_f \otimes \mathbf{u}_f) = -\nabla p + \nabla \cdot \left[\mu_f \left(\nabla \mathbf{u}_f + \nabla \mathbf{u}_f^T \right) - \frac{2}{3} \mu_f (\nabla \cdot \mathbf{u}_f) \mathbf{I} \right] + \mathbf{f}_{TWC}, \quad (2)$$

$$\frac{\partial (\rho_f C_{v,f} T_f)}{\partial t} + \nabla \cdot (\rho_f C_{P,f} T_f \mathbf{u}_f) = \nabla \cdot (\lambda_f \nabla T_f) + S_{TWC}, \quad (3)$$

145 where \mathbf{u}_f is the fluid velocity, \mathbf{I} is the identity matrix, μ_f and λ_f are the dynamic viscosity and thermal
 146 conductivity, and \mathbf{f}_{TWC} and S_{TWC} are two-way coupling terms representing the effect of particles on the
 147 fluid and defined as

$$\mathbf{f}_{TWC} = \sum_p m_p \frac{\mathbf{v}_p - \mathbf{u}_p}{\tau_p} \delta(\mathbf{x} - \mathbf{x}_p) \quad \text{and} \quad S_{TWC} = \sum_p \pi d_p^2 h (T_p - T_f) \delta(\mathbf{x} - \mathbf{x}_p), \quad (4)$$

148 with \mathbf{u}_p the fluid velocity at the particle location, $\tau_p = \rho_p d_p^2 / (18\mu_f)$ the particle relaxation time, d_p and T_p the
 149 particle diameter and temperature, respectively, and $\delta(\mathbf{x} - \mathbf{x}_p)$ the Dirac delta function concentrated at the
 150 particle position. In this work, particles are assumed to be isothermal as their Biot number — $Bi = hd_p/\lambda_p$,
 151 where h the fluid-particle convection coefficient and λ_p the thermal conductivity of particles — is small, i.e.,
 152 $Bi \ll 1$.

153 2.1.2. Lagrangian representation of particles

In this study, the particle sizes are several orders of magnitude smaller than the smallest significant flow
 scale, and the density ratio between particles and fluid is $\rho_p/\rho_f \gg 1$. As a result, particles are modeled
 following a Lagrangian PP approach in which Stokes' drag is the most important force [38]. Their description
 in terms of position, velocity and temperature is given by

$$\frac{d\mathbf{x}_p}{dt} = \mathbf{v}_p, \quad (5)$$

$$\frac{d\mathbf{v}_p}{dt} = \frac{\mathbf{u}_p - \mathbf{v}_p}{\tau_p}, \quad (6)$$

$$\frac{d(m_p C_{v,p} T_p)}{dt} = \frac{\pi d_p^2}{4} \epsilon_p I_0 - \pi d_p^2 h (T_p - T_f), \quad (7)$$

154 where $C_{v,p}$ and ϵ_p are the particle specific isochoric heat capacity and radiation absorption coefficient (an
 155 optically thin medium has been assumed), and I_0 is an uniform intensity irradiating the system. In the
 156 conservation equation for particle temperature (7), the first term on the right-hand-side accounts for the
 157 amount of radiation absorbed by a particle, while the second term represents the heat transferred to its
 158 surrounding fluid.

159 2.2. Computational approach

160 The equations of fluid motion (1-3) are solved following an Eulerian finite-difference discretization imple-
 161 mented in an in-house solver that is second-order accurate in space and suitable to non-uniform Cartesian
 162 meshes. A fourth-order Runge-Kutta scheme is used for integrating the equations in time, together with
 163 a fractional-step method for imposing conservation of mass [39]. Integration in time of the Lagrangian
 164 position, velocity, and temperature of particles (5-7) is fully coupled with the advancement of the flow equa-
 165 tions to achieve fourth-order accuracy. The resulting multiphysics computational flow solver [40, 41] has
 166 been developed, verified & validated, and extensively utilized to study the interaction between turbulent
 167 flow, particle transport and thermal radiation within the Predictive Science Academic Alliance Program
 168 (PSAAP) II at Stanford University [42], which focuses on advancing the state-of-the-art in large-scale, pre-
 169 dictive simulations of irradiated particle-laden turbulence relevant to CSP systems. Selected publications
 170 include (i) the fundamental understanding and characterization of flow mechanisms [17, 18], (ii) subgrid-
 171 scale (SGS) modeling of the carrier and dispersed phases in large-eddy simulation (LES) approaches [43, 44],
 172 the efficient propagation and quantification of uncertainties [11, 12], and the compression and reduction of
 173 high-dimensional systems [13, 14].

174 3. Data-driven dimensional analysis

175 In this section, we describe the integration of classical dimensional analysis with modern dimension reduc-
 176 tion techniques. The resulting tools¹ enable data-driven discovery of relevant dimensionless numbers, while

¹The Python package `pybuck` [45] has been built and released to support the concepts introduced in this section.

177 accounting for the practical realities of large-scale simulations. The following subsections detail requisite
 178 background material.

179 3.1. Dimensional analysis and the π subspace

180 To enable data-driven dimensional analysis, we first connect classical techniques to a modern subspace
 181 reduction perspective. Dimensional analysis is a classical dimension reduction technique [22]. Its central
 182 result is the Buckingham π theorem, which postulates: Given a set of dimensional inputs $\mathbf{z} \in \mathbb{R}^{n_d}$ that
 183 predict a dimensionless QoI, i.e., $Q = f(\mathbf{z})$, the functional relationship may be re-expressed in terms of a
 184 smaller number of dimensionless numbers $\boldsymbol{\pi} \in \mathbb{R}^{n_p}$ via $\pi = \psi(\pi_1, \dots, \pi_{n_p})$. The set of valid dimensionless
 185 inputs $\boldsymbol{\pi} = \{\pi_1, \dots, \pi_{n_p}\}$ can be determined from the *dimension matrix* \mathbf{D} . Following the notation of del
 186 Rosario et al. [32], let $\mathbf{d}(\cdot)$ be a vectorization of the dimension function [46]. Then, the dimension matrix
 187 for \mathbf{z} is given by

$$\mathbf{D} = [\mathbf{d}(\mathbf{z}_1), \dots, \mathbf{d}(\mathbf{z}_{n_d})]. \quad (8)$$

188 As an illustrative example, consider the physical input quantities for Osborne Reynolds’ classic 1883 pipe
 189 flow experiment [47]: fluid density ρ_F , bulk velocity U_F , dynamic viscosity μ_F , pipe diameter d_P , and
 190 roughness lengthscale ϵ_P . Table 1 gives the dimension matrix and a valid set of dimensionless numbers for
 191 this setting.

	ρ_F	U_F	d_P	μ_F	ϵ_P
<u>Dimension:</u>					
Mass (M)	1	0	0	1	0
Length (L)	-3	1	1	-1	1
Time (T)	0	-1	0	-1	0
Temperature (H)	0	0	0	0	0
<u>Group:</u>					
Reynolds number (Re)	1	1	1	-1	0
Relative roughness (r)	0	0	-1	0	1

Table 1: Dimension matrix \mathbf{D} and a basis for the π subspace (nullspace of \mathbf{D}) for Reynolds’ pipe flow. The Dimension entries define the dimension matrix for the pipe flow setting, which has shape $\mathbf{D} \in \mathbb{R}^{4 \times 5}$. Each column of \mathbf{D} encodes the physical dimensions of an input; for instance we have $[\rho_F] = M^1 L^{-3} T^0 H^0$. Since the Temperature (H) row is identically zero, the rank of \mathbf{D} is 3. The Buckingham π theorem indicates the size of the π subspace is $5 - 3 = 2$ dimensional. A standard choice of basis for this two-dimensional π subspace is the Reynolds number $\pi_1 = Re = \rho_F^1 U_F^1 d_P^1 \mu_F^{-1} \epsilon_P^0$ and relative roughness $\pi_2 = r = \rho_F^0 U_F^0 d_P^{-1} \mu_F^0 \epsilon_P^1$.

192 Valid dimensionless numbers can be formed by products of the inputs as

$$\pi_i = \prod_{j=1}^{n_d} z_j^{v_{ij}}, \quad (9)$$

193 with the vectors $\{\mathbf{v}_j\}_{j=1}^{n_p}$ satisfying $\mathbf{D}\mathbf{v}_j = 0$. In this formulation, the Buckingham π theorem can be
 194 understood in terms of the rank-nullity theorem. In other words, the number of independent dimensionless
 195 numbers — with independence defined by the usual notion of vector independence applied to \mathbf{v}_i — is given
 196 by

$$n_p = \dim[\mathcal{R}(\mathbf{D})] - \dim[\mathcal{N}(\mathbf{D})], \quad (10)$$

197 where $\dim[\cdot]$ is the subspace dimension, $\mathcal{R}(\cdot)$ denotes the range, and $\mathcal{N}(\cdot)$ denotes the nullspace. The
 198 Buckingham π theorem is silent on the *choice of a basis* for the nullspace of \mathbf{D} (i.e., set of dimensionless
 199 groups); for the Reynolds’ pipe flow case, a standard choice is the Reynolds number $Re = \rho_F U_F d_P / \mu_F$
 200 and relative roughness $r = \epsilon_P / d_P$. The choice of “appropriate” dimensionless numbers is often a matter of
 201 experience. However, in this work we use data to inform a useful selection of relevant $\boldsymbol{\pi}$ groups.

202 To connect Buckingham’s π theorem to subspace reduction, we make the following observation. Select a
 203 set of nominal conditions $\mathbf{z}_0 \in \mathbb{R}^{n_d}$ and define $x_i = \log(z_i/z_{i,0})$ for $i = 1, \dots, n_d$. Under this transform, we
 204 can write

$$\begin{aligned} \pi &= \psi \left\{ \exp[\mathbf{v}_1^\top \mathbf{x}_1 + \log(\pi_{1,0})], \dots, \exp[\mathbf{v}_{n_p}^\top \mathbf{x}_{n_p} + \log(\pi_{n_p,0})] \right\}, \\ &= \psi' [\mathbf{V}^\top \mathbf{x} + \log(\boldsymbol{\pi}_0)], \end{aligned} \quad (11)$$

205 where $\mathbf{V} = [\mathbf{v}_1, \dots, \mathbf{v}_{n_p}]$ and $\pi_{i,0}$ are the dimensionless numbers evaluated at the constant nominal condi-
 206 tions $z_{i,0}$, $\boldsymbol{\pi}_0 = [\pi_{1,0}, \dots, \pi_{n_p,0}]^\top$, and the composition exponentiation is collapsed within ψ' to highlight
 207 mathematical structure. Intuitively, this structure exhibits variability only within a subspace of its input
 208 domain, and is invariant to orthogonal perturbations. Note that the choice of nominal conditions \mathbf{z}_0 enters
 209 into (11) only through the offset $\boldsymbol{\pi}_0$. One may safely choose \mathbf{z}_0 to be unity in the appropriate units, which
 210 will set all the $\log(\boldsymbol{\pi}_{i,0}) = 0$. The choice of \mathbf{z}_0 above can be thought of as analogous to a Coulomb gauge [48].

211 From (11), one can show that variation in the QoI occurs only through variations within $\mathcal{R}(\mathbf{V})$; since
 212 this object is derived from Buckingham’s π theorem, it is called the π *subspace* [32]. Note that the QoI
 213 must be non-dimensionalized for this property to hold; if the QoI is dimensional, then the slightly larger
 214 *dimensional analysis subspace* is the relevant object [33]. To elucidate the importance of the π subspace, let
 215 $\mathcal{R}(\mathbf{V})^\perp$ be the orthogonal complement of $\mathcal{R}(\mathbf{V})$, and let $\mathbf{y} \in \mathcal{R}(\mathbf{V})^\perp$. Then

$$\begin{aligned} \pi(\mathbf{x} + \mathbf{y}) &= \psi' [\mathbf{V}^\top (\mathbf{x} + \mathbf{y})], \\ &= \psi' [\mathbf{V}^\top \mathbf{x} + \mathbf{0}], \\ &= \pi(\mathbf{x}), \end{aligned} \quad (12)$$

216 making precise the previous statement of invariance. This invariance shows that (11) is a *ridge function* in
 217 its inputs \mathbf{x} [34]. A restatement of this invariance is that the gradient of π is constrained. In mathematical
 218 form, note that

$$\nabla_{\mathbf{x}} \pi = \mathbf{V} \nabla_{\boldsymbol{\xi}} \psi'(\boldsymbol{\xi}), \quad (13)$$

219 and as a result the following relation is satisfied

$$\nabla_{\mathbf{x}} \pi \in \mathcal{R}(\mathbf{V}). \quad (14)$$

220 This observation will prove useful as we discuss active subspaces below. Note that while Buckingham’s π
 221 theorem defines a set of valid dimensionless numbers — equivalently the π subspace $\mathcal{R}(\mathbf{V})$ — it does not
 222 provide a specific choice of an appropriate basis \mathbf{V} [33]. The function ψ' may have additional structure with
 223 further invariance properties. These properties can be expressed in terms of active subspaces.

224 3.2. Active subspaces and dimensional analysis

225 The active subspace is a dimension reduction concept introduced by Russi [49] and developed by Con-
 226 stantine [36]. Let $f(\mathbf{x})$ be some differentiable QoI on a domain with integral weight $\rho(\mathbf{x}) \in \mathbb{R}_{\geq 0}$. The active
 227 subspace is then defined in terms of the matrix

$$\mathbf{C} \equiv \int \nabla_{\mathbf{x}} f \nabla_{\mathbf{x}} f^\top \rho(\mathbf{x}) d\mathbf{x}. \quad (15)$$

228 The integral weight $\rho(\mathbf{x})$ must be chosen by the analyst to select and emphasize the regions of the input
 229 space that are of practical interest. In this work, we construct $\rho(\mathbf{x})$ by selecting bounds for the inputs (e.g.,
 230 Table 3) and choosing a uniform weight. Since \mathbf{C} is by construction symmetric semi-positive definite, it
 231 admits an eigenvalue decomposition of the form $\mathbf{C} = \mathbf{U} \boldsymbol{\Lambda} \mathbf{U}^\top$. The eigenvalues need to be sorted first in
 232 decreasing order as $\lambda_1 \geq \dots \geq \lambda_{n_d}$. Next, a threshold separating $\{\lambda_1, \dots, \lambda_{n_d}\}$ into large $\{\lambda_1, \dots, \lambda_{n_A}\}$
 233 and small $\{\lambda_{n_A+1}, \dots, \lambda_{n_d}\}$ eigenvalues is defined to generate the split $\mathbf{U} = [\mathbf{U}_A, \mathbf{U}_I]$. The final result is
 234 that the directions \mathbf{u}_i are then ordered in decreasing order of “importance” with respect to variation in the
 235 QoI f , made quantitative by the eigenvalues, which is equivalent to the mean-squared directional derivative

236 along direction \mathbf{u}_i [36]. The *active subspace* is then given by $\mathcal{R}(\mathbf{U}_A)$, where the columns of \mathbf{U}_A form a basis
 237 for the subspace.

238 In the case where f represents a physical equation respecting dimensional homogeneity, Buckingham's π
 239 theorem guarantees the range constraint in (14). From this fact, it is clear that if $\mathbf{w} \in \mathcal{R}(\mathbf{V})^\perp$, we have

$$\mathbf{w}^\top \mathbf{C} \mathbf{w} = \mathbb{E}[\mathbf{w}^\top \nabla_{\mathbf{x}} f \nabla_{\mathbf{x}} f^\top \mathbf{w}] = 0, \quad (16)$$

240 where $\mathbb{E}[\cdot]$ denotes the expectation operator, using the same integral weight $\rho(\mathbf{x})$ as (15). An immediate
 241 consequence of this nullity is that if one requires the active subspace to include only those directions for
 242 which $\lambda_i > 0$, then

$$\mathcal{R}(\mathbf{U}_A) \subseteq \mathcal{R}(\mathbf{V}). \quad (17)$$

243 In words, the active subspace, computed along the transformed variables \mathbf{x} , is a subset of the π subspace.
 244 Furthermore, using the vector entries in (9), the active directions $\mathbf{u}_{A,i}$ can be directly interpreted as dimensionless
 245 groups.

246 The selection of the active subspace dimension n_A requires some caution. If $f(\mathbf{x}) = g(\mathbf{V}^\top \mathbf{x})$ is a ridge
 247 function in its inputs \mathbf{x} , then one can use property (12) to show that $\lambda_i = 0$ for $i > \dim[\mathcal{R}(\mathbf{V})]$; thus,
 248 $n_A \leq \dim[\mathcal{R}(\mathbf{V})]$. However, one may also make a ‘‘pragmatic’’ choice of n_A based on preserving a user-
 249 defined level of variance in the function [50]. We illustrate navigating these challenges in the subsection
 250 below.

251 3.3. Using data-driven dimensional analysis

252 Using active subspaces together with dimensional analysis enables a number of investigative approaches.
 253 The active directions can be used to produce a *summary plot* of the input-to-output response [51]. A
 254 summary plot consists of a plot of the response f_i against reduced coordinates $\xi_A \equiv \mathbf{U}_A^\top \mathbf{x}_i$. In the case
 255 where $\dim(\mathbf{U}_A) = 1$, this can be easily visualized as a scatter plot, while $\dim(\mathbf{U}_A) = 2$ can be plotted with
 256 additional difficulty as a value-colored scatter plot. Figure 1 gives an example of the one-dimensional (1-D)
 257 case for the familiar setting of Reynolds' pipe flow. This figure highlights the connections between the usual
 258 mechanics of dimensional analysis and the language of dimension reduction.

259 Even when the active subspace is too high dimensional to be directly visualized, the active directions
 260 \mathbf{U}_A can be directly re-interpreted by *re-expressing* them in terms of a user-supplied basis of interpretable
 261 dimensionless numbers. Data-driven dimensional analysis identifies $\boldsymbol{\pi}$ groups which are relevant to the data
 262 at hand, but the resulting products of inputs need not involve ‘‘simple’’ powers. Conversely, the common
 263 dimensionless numbers, such as the Reynolds number, Mach number, and Prandtl number, carry physical
 264 interpretation; generally, ratios of competing effects. Re-expressing a given active direction \mathbf{u} in a user-
 265 defined basis \mathbf{V} of these interpretable dimensionless numbers is useful for physically interpreting the results.
 266 In practice, if one solves a linear system for weights \mathbf{w} via

$$\mathbf{V} \mathbf{w} = \mathbf{u}, \quad (18)$$

267 then, the dimensionless groups represented by \mathbf{u} can be re-expressed as

$$\begin{aligned} \pi &= \exp(\mathbf{u}_d^\top \mathbf{x}), \\ &= \exp(\mathbf{w}^\top \mathbf{V}^\top \mathbf{x}), \\ &= \exp\left[w_1(\mathbf{v}_1^\top \mathbf{x}) + \cdots + w_{n_p}(\mathbf{v}_{n_p}^\top \mathbf{x})\right], \\ &= \pi_1^{w_1} \times \cdots \times \pi_{n_p}^{w_{n_p}}. \end{aligned} \quad (19)$$

268 This allows one to construct data-driven dimensionless groups from a user-selected basis of ‘‘standard’’
 269 dimensionless numbers, greatly aiding in physical interpretation.

270 One additional application of data-driven dimensional analysis is the detection of ‘‘unknown’’ unknowns,
 271 so-called *lurking variables* [53]. If an analyst is unaware of important physical variables that affect a physical
 272 QoI, then the neglected variables are said to be lurking. As a concrete example of a lurking variable, note

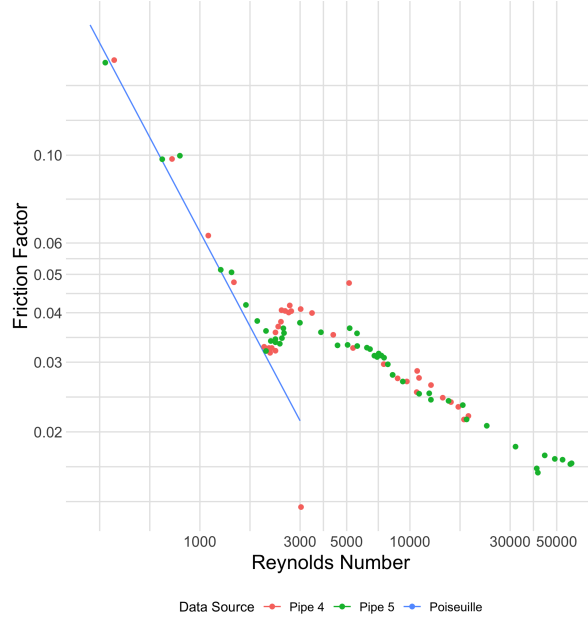


Figure 1: Reynolds' pipe flow data of friction factor versus Reynolds number. In the language of dimension reduction, this is a *summary plot*, viz. a visualization of a response f_i against a reduced coordinate $\mathbf{v}_{Re}^\top \mathbf{x}_i$. The choice of weights \mathbf{v}_{Re} corresponds to the Reynolds number; referencing against Table 1 gives $\mathbf{v}_{Re} = [+1, +1, +1, -1, 0]^\top$. Here the data are well explained by the Reynolds number, particularly for the low-Reynolds ($Re < 2000$) cases. However, it is well known that in turbulent flows the effects of wall roughness becomes important, requiring another dimensionless number to adequately explain the variation in the friction factor [52].

273 that in Osborne Reynolds' original 1883 experiment, he was unaware of the importance of pipe roughness
 274 ϵ_P . While Reynolds employed the *method of concentrated staring* [54] to detect the presence of a lurking
 275 variable, we will briefly describe here how one can detect lurking variables *automatically* with data-driven
 276 dimensional analysis [32].

277 We introduce a formal split between *exposed* \mathbf{x}_E and *lurking* variables \mathbf{x}_L , and without loss of generality
 278 write

$$\begin{aligned} \mathbf{x}^\top &= [\mathbf{x}_E^\top, \mathbf{x}_L^\top], \\ \nabla_{\mathbf{x}} \pi &= [\nabla_{\mathbf{x}_E} \pi^\top, \nabla_{\mathbf{x}_L} \pi^\top]. \end{aligned} \quad (20)$$

279 Using (13), we note that $\nabla_{\mathbf{x}} \pi = \mathbf{V} \nabla_{\mathbf{y}} \psi'(y)$, thus we have

$$\begin{aligned} 0 &= \mathbf{D} \nabla_{\mathbf{x}} \pi, \\ 0 &= \mathbf{D} [\nabla_{\mathbf{x}_E} \pi^\top, \nabla_{\mathbf{x}_L} \pi^\top]^\top, \\ \mathbf{D} \nabla_{\mathbf{x}_E} \pi &= -\mathbf{D} \nabla_{\mathbf{x}_L} \pi. \end{aligned} \quad (21)$$

280 The situation where lurking variables exist corresponds to the setting where analysts believe they have \mathbf{x} ,
 281 but in reality have \mathbf{x}_E . Thus, in practice analysts may compute $\mathbf{D}_E \nabla_{\mathbf{x}_E} \pi$ and check if this quantity is equal
 282 to zero. If this quantity is nonzero, it signals that lurking variables may exist, and gives a hint as to what
 283 physical units those lurking variables may have.

284 We note briefly that lurking variables are typically not a problem in computer simulations, unless one
 285 is working with legacy black-box codes. In practice, we have used the above techniques as a form of error-
 286 checking. In the case of computer simulations, where the resulting active directions have nonzero excess
 287 physical dimensions $\mathbf{D}\mathbf{u}$, this signals that either: (i) lurking variables exist, or (ii) there is a mistake in the
 288 computations. However, note that while lurking variables may not afflict a code, any variables which are
 289 not varied in the computation, but contribute to the dimensional homogeneity of the governing equations,

290 qualify as so-called *pinned quantities*. These neglected quantities must be accounted when performing checks
 291 for excess physical dimensions as comprehensively explained in del Rosario et al. [32].

292 3.4. Approximating and evaluating active subspaces

293 Studying active subspaces is further complicated by the realities of approximation. Generally, (15) cannot
 294 be computed exactly. Direct approximation of (15) requires evaluation, or approximation, of the gradient
 295 $\nabla_{\mathbf{x}}f$ — finite differences increase the computational complexity of simulation by a factor $d+1$; in our target
 296 application, this corresponds to an order-of-magnitude increase.

297 Rather than approximating the matrix (15) directly, we instead leverage recent algorithms using *variable*
 298 *projection* [35]. Conceptually, this procedure embeds a least-squares polynomial approximation within an
 299 optimization over the Grassmann manifold. The need for gradient data $\nabla_{\mathbf{x}}f$ is ameliorated by assuming a
 300 polynomial model form and target dimensionality, allowing gradient approximation based on the assumed
 301 model. In this way, one may use point evaluations $f(\mathbf{x}_i)$ in place of gradient samples $\nabla_{\mathbf{x}}f_i$, greatly reducing
 302 computational expense.

303 Here we review the *principal angles* to help measure subspace alignment and assess an estimated active
 304 subspace in the dimensional analysis context [55]. Let $\mathcal{F}, \mathcal{G} \subseteq \mathbb{R}^m$ be subspaces with

$$p = \dim(\mathcal{F}) \geq \dim(\mathcal{G}) = q \geq 1. \quad (22)$$

305 The *principal angles* $\{\theta_i\}_{i=1}^q$ are defined recursively via

$$\cos(\theta_k) = \mathbf{f}_k^\top \mathbf{g}_k = \max_{\mathbf{f} \in \mathcal{F}} \max_{\mathbf{g} \in \mathcal{G}} \mathbf{f}^\top \mathbf{g}, \quad (23)$$

306 where \mathbf{f}_k and \mathbf{g}_k are required to be mutually orthogonal and of unit length. Note that the angles satisfy
 307 $0 \leq \theta_1 \leq \dots \leq \theta_q \leq \pi/2$, and if $\theta_i = 0$ then $\mathbf{f}_i = \mathbf{g}_i$. For convenience, we denote the maximum principal
 308 angle by $\theta_{\max} = \max_{i=1, \dots, q} \theta_i$.

309 Since $\dim[\mathcal{R}(\mathbf{U}_A)] \leq \dim[\mathcal{R}(\mathbf{V})]$, we set $\mathcal{F} = \mathcal{R}(\mathbf{V})$ and $\mathcal{G} = \mathcal{R}(\mathbf{U}_A)$. Theorem 6.4.2 of Golub & Van
 310 Loan [55] characterizes the intersection of two subspaces in terms of the zero principal angles (if any exist);
 311 the principal directions $(\mathbf{f}_i, \mathbf{g}_i)$ corresponding to the zero-angles form a basis for the intersection. Given
 312 the inclusion characterization of (17), we expect the maximum principal angle between the active and π_i
 313 subspaces to be zero. However, an *estimated* active subspace may fail to lie within the π subspace. We
 314 may use the maximum subspace angle θ_{\max} to characterize the accuracy of the estimated subspace. If this
 315 angle is significantly nonzero, then either lurking variables or implementation issues afflict the computation.
 316 Determining the meaning of “significantly” requires some care. We frame this question in terms of classical
 317 significance testing with a null hypothesis of $H_0 : \theta_{\max} = 0$. Rather than compute p-values, we approximate
 318 confidence intervals on θ_{\max} via the standard bootstrap table method [56]. The case when these confidence
 319 intervals include zero is compatible with H_0 , while the case when the interval excludes zero indicates the
 320 possible pathologies mentioned above.

321 As an illustrative example, we describe the detection of lurking variables on the Reynolds’ pipe flow
 322 example introduced above. We consider two settings, one with the nominal Reynolds number less than
 323 critical [Laminar, $Re \sim \mathcal{O}(10^2)$], and the other with the nominal Reynolds number larger than the critical
 324 value [Turbulent, $Re \sim \mathcal{O}(10^7)$]. In both cases, we build a dataset utilizing the simple computational model
 325 described in Section 2 of del Rosario et al. [32], in which all but the roughness lengthscale ϵ_P are allowed
 326 to vary, and seek a 1-D active subspace using a first-order polynomial fit. This simple case reduces to
 327 ordinary least squares regression. Applying the bootstrap and approximating subspace angle confidence
 328 intervals yields the results provided in Table 2. As it is shown, there are no lurking variables in the Laminar
 329 case, and as a result the confidence interval includes zero. In the Turbulent case, however, the roughness
 330 lengthscale is (by construction) missing from the computation, and consequently the confidence interval is
 331 far separated from zero. The latter case provides strong evidence for lurking variables, while the former
 332 case gives results compatible with no lurking variables. This sort of diagnostic tool can aid interpretation
 333 of data-driven dimensional analysis results, particularly the detection of errors.

	Lower	Upper	M	L	T
Laminar	-0.02	+0.02	-0.03	+0.04	+0.02
Turbulent	+0.71	+0.71	+0.00	-0.53	+0.00

Table 2: Table of subspace angle bootstrap 95% confidence intervals for the Reynolds’ pipe flow example. Both cases consider the roughness ϵ_P fixed. In the Laminar case, the lower and upper bounds for the subspace angle confidence interval include zero, indicating that no lurking variables are detected. In the Turbulent case, the confidence interval excludes zero, providing evidence for the presence of a lurking variable. The last three columns provide the physical dimensions of the test statistics. In the Turbulent case, the detected lurking variable is estimated to have units of length, corresponding correctly with the missing ϵ_P parameter.

334 4. Description of the irradiated particle-laden turbulence system

335 The setup of the problem is inspired by the study of thermo-fluid mechanisms in volumetric particle-based
336 solar energy receivers. As illustrated in Figure 2, the analysis of this type of system involves the interaction
337 of particles, turbulent flow and radiative heat transfer. The instantaneous snapshot, extracted from a PP-
338 DNS with physical particles, corresponds to the normalized temperature increment, $\Delta T/T_0 = (T - T_0)/T_0$,
339 of fluid and particles on the xy -plane along the streamwise direction. A complete description of the problem
340 setup and system parameters is presented in the subsections below.

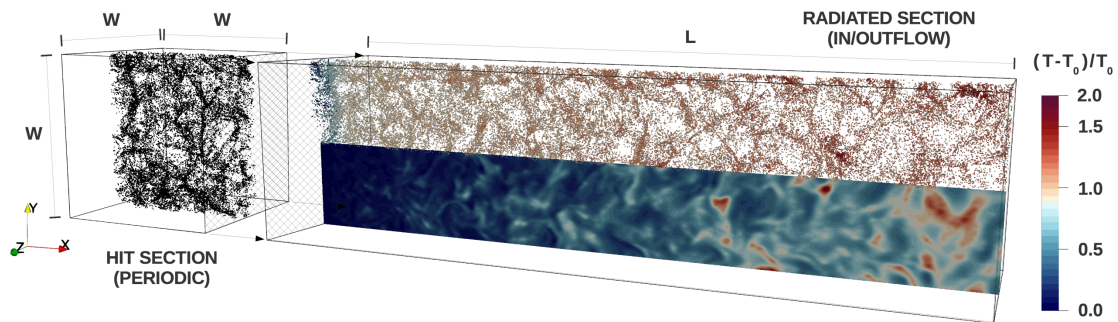


Figure 2: Setup of the problem. The forced HIT (left) domain is utilized to provide fluid-particle inflow conditions to the radiated (right) section. The color scheme indicates normalized temperature increment, $\Delta T/T_0$, of the particle (top) and fluid (bottom) phases (instantaneous xy -plane).

341 4.1. Problem setup

342 The study of particle-laden turbulence in an irradiated environment is performed by considering the
343 two domains depicted in Figure 2. The cubic domain of size W is an isothermal, particle-laden HIT flow
344 generator in which the fluid phase (initial density $\rho_{0,f}$ and temperature $T_{0,f}$, constant dynamic viscosity
345 μ_f) is volumetrically forced [57]. The dispersed phase is initialized at the same time and temperature as the
346 fluid with $N_{p,0}$ monodisperse particles (constant density ρ_p and diameter d_p) randomly distributed in the
347 volume. The turbulence forcing scheme is targeted to produce an averaged turbulent kinetic energy, $k_{\infty,f}$,
348 such that the ratio between domain size and Kolmogorov length scale, η , is $W/\eta \sim \mathcal{O}(10^2)$, and therefore
349 the small-scale features of the flow are not significantly affected by the triply periodic boundaries. This first
350 domain is designed to provide turbulent steady-state fluid-particle inflow conditions to the (second) radiated
351 section.

352 The rectangular radiated section is of size $L \times W \times W$ in the streamwise (x , in/outflow boundaries),
353 spanwise (y , periodic boundaries) and crossflow (z , periodic boundaries) directions, respectively. The tur-
354 bulent fluid-particle flow mixture is sampled in time from a yz -plane in the HIT volume and introduced
355 to this second domain by adding a bulk velocity U_0 to the streamwise velocity component. To achieve
356 similar turbulence characteristics as in wall-bounded flows, the ratio between root-mean-square velocity
357 fluctuations, u_{rms} , in the HIT domain and U_0 is selected to be $u_{rms}/U_0 \sim \mathcal{O}(10^{-1})$, and the gravitational

Parameter	Value	Parameter	Value
W	[0.038 : 0.042] m	$C_{P,f}/C_{v,f}$	1.4 (diatomic ideal gases)
L	[0.152 : 0.168] m	h	[$1 \cdot 10^3$: $1 \cdot 10^4$] W/(m ² · K)
T_0	[285 : 315] K	$N_{p,0}$	[$9.5 \cdot 10^{5,6}$: $10.5 \cdot 10^{5,6}$]
U_0	[1 : 5] m/s	ρ_p	[$1 \cdot 10^3$: $1 \cdot 10^4$] kg/m ³
$k_{\infty,f}$	[0.1 : 0.5] m ² /s ²	d_p	[$1 \cdot 10^{-6}$: $1 \cdot 10^{-5}$] m
$\rho_{f,0}$	[0.5 : 1.5] kg/m ³	$C_{v,p}$	[$1 \cdot 10^2$: $1 \cdot 10^3$] J/(kg · K)
μ_f	[$1 \cdot 10^{-5}$: $2 \cdot 10^{-5}$] Pa · s	ϵ_p	[0.25 : 0.75]
λ_f	[$1 \cdot 10^{-2}$: $3 \cdot 10^{-2}$] W/(m · K)	I_0	[$9.5 \cdot 10^5$: $10.5 \cdot 10^5$] W/m ²
$C_{P,f}$	[$1 \cdot 10^3$: $2 \cdot 10^3$] J/(kg · K)		

Table 3: List of independent input parameters with their range of values.

358 acceleration is not considered as its effects are negligible compared to the inertia of the bulk flow. As the
359 fluid-particle mixture flows through the domain, it is irradiated with uniform intensity I_0 . The result is
360 that particles (constant isochoric heat capacity $C_{v,p}$ and absorption coefficient ϵ_p) absorb thermal radiation,
361 increasing their temperature, T_p , and subsequently transferring energy to the surrounding fluid (constant
362 thermal conductivity λ_f and isobaric heat capacity $C_{P,f}$) by thermal exchange (constant fluid-particle heat
363 convection coefficient h).

364 The fluid-particle mixture in this problem is optically thin, allowing us to model the radiation absorption
365 by particles with the algebraic model described in Section 2; in other words, all particles receive the same
366 amount of radiation intensity. As a result of the particles heating and transferring thermal energy to the
367 carrier fluid, the average fluid temperature \bar{T}_f increases along the streamwise direction. This deposition of
368 energy accelerates the flow by means of thermal expansion due to a decrease in fluid density ρ_f .

369 4.2. System parameters

370 The computational study conducted in this work is designed with the objective of mimicking an experi-
371 ment as it would be carried out in a laboratory facility. Following this approach, the system is characterized
372 by 16 input parameters that can be varied independently to collect data. The list of input parameters and
373 their range of values are described in Table 3. The ranges of W , L , T_0 , and I_0 are obtained by adding 5%
374 to/subtracting 5% from their nominal values as these are parameters that in a laboratory facility would not
375 be easily modified in large proportions. The intervals for $\rho_{f,0}$, μ_f , λ_f , $C_{P,f}$, h , ρ_p , $C_{v,p}$, and ϵ_p are based on
376 engineering values for material properties taken from Poling et al. [58]; the generic fluid is considered to be
377 a diatomic ideal gas resulting in $C_{P,f}/C_{v,f} = 1.4$. The levels of U_0 and $k_{\infty,f}$ are designed together to obtain
378 realistic ratios of fluctuating-to-bulk velocity in turbulent wall-bounded flows [59]. Finally, the ranges of d_p
379 and $N_{p,0}$ are selected to study micron-sized particles representative of conditions in volumetric particle-based
380 solar receivers at relatively small (case I: $N_{p,0} = 1 \cdot 10^6 \pm 5\%$) and large (case II: $N_{p,0} = 1 \cdot 10^7 \pm 5\%$) particle
381 number densities, $n_{p,0}$.

382 Data are collected by computing PP-DNS of the problem for different values of the input parameters
383 sampled from a randomized Halton sequence [60]. For each case (I and II), 128 samples have been computed;
384 a convergence study indicated that above 96 samples the relative convergence error is below 10^{-3} . The range
385 of values for W , L , and $k_{\infty,f}$ are utilized to define, following the estimations described by Pope [59], the mesh
386 resolution required to perform the calculations such that all the significant turbulent scales are captured.
387 The resulting Eulerian meshes for the HIT and radiated domains correspond to uniform Cartesian grids of
388 sizes $512 \times 512 \times 512$ and $2048 \times 512 \times 512$, respectively. The time-averaging of the QoIs is computed by
389 taking the ensemble average of 15 flow-through times (FTTs), defined as $\text{FTT} \approx L/U_0$, on yz -planes — the
390 solution is symmetric in the y and z directions — after the first thermal transient FTT is surpassed.

391 5. Results and discussion

392 This section presents and analyzes the data acquired by computing the set of samples described in Sec-
393 tion 4, and provides a discussion of the results obtained from the methodology introduced in Section 3. A

394 concise characterization of the thermo-fluid mechanisms encountered in the irradiated particle-laden turbu-
 395 lence system is performed first in Section 5.1. Next, in Section 5.2, principal π groups are inferred from the
 396 data generated by utilizing the methodology presented in Section 3. Finally, the π groups are re-expressed
 397 on a “standard” fluid mechanics basis and interpreted from a physics perspective in Section 5.3.

398 5.1. Thermo-fluid characterization of the system

399 The distribution of fluid and particles in the radiated section plays an important role in determining
 400 how radiation interacts with the system. Three principal kinematic scales are responsible for the resulting
 401 distribution: (i) bulk velocity U_0 ; (ii) slip velocity of particles, exhibiting largest values of order $u_p - v_p \sim$
 402 $\sqrt{\varepsilon\tau_p}$ [61] at the viscous-dominated scales with ε the turbulent dissipation rate; and (iii) root-mean-square
 403 of the turbulent velocity fluctuations $u_{rms} = \sqrt{(2/3)k_{\infty,f}}$.

404 The bulk velocity imposes the large scale of the flow in the radiated domain; by construction, U_0 is on
 405 average an order of magnitude larger than the turbulent fluctuations and the slip velocities generated in the
 406 HIT domain. Consequently, the residence time of the fluid-particle mixture in the radiated section is (to a
 407 first-order approximation) directly proportional to this velocity scale, viz. a fluid-particle element will be
 408 exposed to radiation and able to absorb radiative energy for a characteristic time comparable to a FTT.
 409 This velocity scale is an input parameter in the problem that has been designed, in combination with u_{rms} ,
 410 to be representative of bulk turbulence in wall-bounded flows. However, the interaction of the system with
 411 radiation notably increases the streamwise velocity of the carrier and dispersed phases for all samples, and
 412 as a result the residence time decreases in significant proportions. Figure 3 depicts this effect in terms of
 413 normalized time-averaged streamwise fluid velocity, i.e., $(\bar{u}_f - U_0)/U_0$, for I (a) and II (b). In particular, as
 414 the fluid-particle mixture is advected through the radiated domain, the average velocity increases following
 415 a logarithmic trajectory with maximum mean increments of $(\bar{u}_f - U_0)/U_0 \approx 0.5$ (I), 0.75 (II) at $x/L = 1$.
 416 In both cases, the statistical variance monotonically increases as more radiative energy is absorbed by the
 417 system; the distributions present coefficients of variation (CoV) of order unity, i.e., $\text{CoV} = \mathbb{V}^{1/2}[Q]/\mathbb{E}[Q] \sim 1$,
 418 and are skewed toward large positive increments.

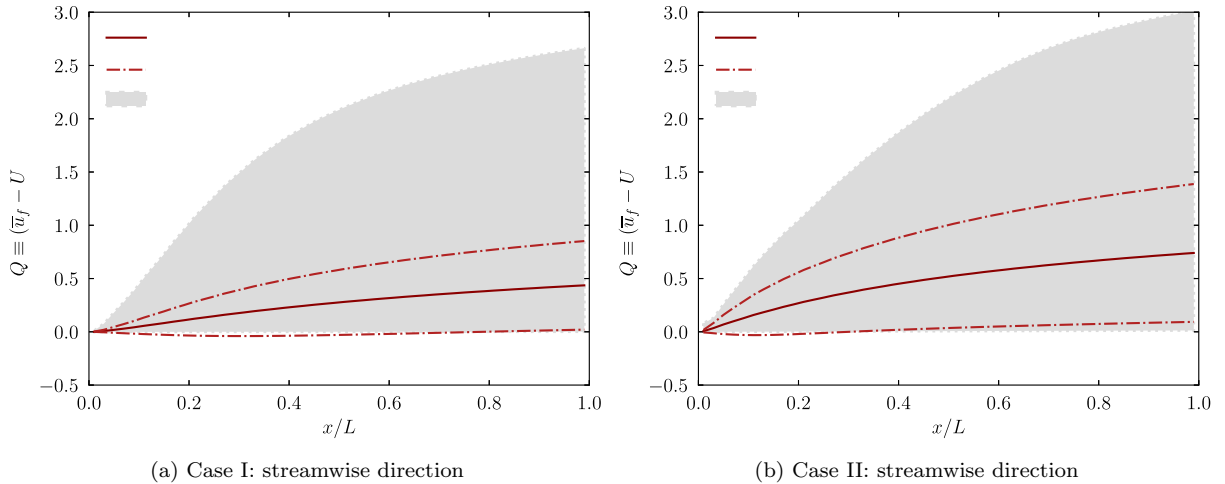


Figure 3: Distribution of normalized u_f -velocity increment along the streamwise direction for I (a) and II (b). Solid lines correspond to the mean of the distributions, dashed lines indicate one standard deviation, and filled regions show the envelope of all samples.

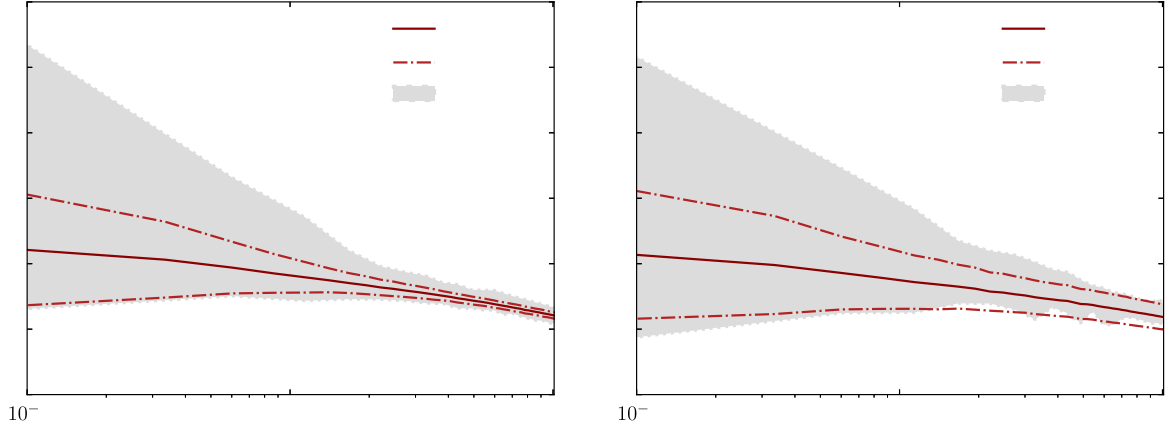
419 The slip velocity of particles with respect to fluid motions determines their spatial organization in
 420 turbulent flows. In the case of inertial particles, small slip velocities result in fairly homogeneous particle
 421 distributions. Instead, as shown in Figure 2, large inter-phase velocity differences generate macroscopic
 422 spatial inhomogeneities by preferentially concentrating the dispersed phase in high-entropy flow locations,

423 i.e., heavy particles are expelled from vortical structures and accumulate in regions where the fluid dissipates
 424 relatively large amounts of kinetic energy. Therefore, for the problem studied in this work, the bulk velocity
 425 U_0 is responsible for the large-scale uniform advection of particles, while their fine-grain distribution is
 426 governed by the slip velocity between phases. This latter mechanism has a direct impact on the inter-
 427 phase energy exchange by determining the surface area to volume ratio of particle clusters; the larger this
 428 ratio, the larger is the radiative power transferred to the fluid surrounding the particles. For example, a
 429 perfectly homogeneous spatial distribution of particles would present, potentially, the largest rate of energy
 430 exchange by maximizing the amount of particle transfer area per unit of fluid volume. In this regard,
 431 particle clustering patterns are typically quantified by means of radial distribution functions (RDF) [62],
 432 which measure the ratio of the number of particle pairs found at a given separation distance to the expected
 433 number if the particles were uniformly distributed. For a given streamwise location, it is assumed that all
 434 particles found within a thin slab are located on the same two-dimensional (2-D) crossflow plane [18]. Under
 435 this assumption, the RDF can be computed for a set of M particles by binning them according to their
 436 separation distance and calculating

$$g(r) = \frac{N_r/A_r}{N/A}, \quad (24)$$

437 where N_r is the number of particle pairs in a disc element with area A_r and radius r from a test particle
 438 location, $N = M(M - 1)/2$ is the total number of particle pairs on the plane, and $A = W^2$ is the total
 439 cross-sectional area. Figure 4 shows the time-averaged particles RDF for I at the inlet (a) and outlet (b)
 440 of the radiated domain for a slab of thickness $\Delta x/\eta = 10$; the results for II follow the same trends as
 441 for I, and they have been consequently omitted. The shape and orders of magnitude of the RDFs at the
 442 inlet and outlet locations are remarkably similar: (i) the mean of the distributions achieve $g(r/\eta) \approx 2$ at
 443 distances smaller than the Kolmogorov scale η , indicating a twofold particle clusterization with respect to
 444 a uniform distribution, whereas they become significantly homogeneous at distances of order $r/\eta \sim 10$ by
 445 reducing to $g(r/\eta) \approx 1$; (ii) the statistical variance transitions from $\text{CoV} \approx 1$ at $r/\eta \sim 0.1$ to $\text{CoV} \ll 1$
 446 at $r/\eta \sim 10$, denoting that the system experiences much more stochastic dispersion at the small scales
 447 which, as discussed in the lines above, translates into large variability in the inter-phase energy exchange
 448 between samples; (iii) the distributions are skewed toward higher $g(r/\eta)$ values, especially for $r/\eta < 1$. This
 449 similarity between RDFs at the inlet and outlet, which has also been reported by Jin et al. [63], Pouransari et
 450 al. [17] and Rahmani et al. [18], is a consequence of particle clusters not being largely affected by the decay
 451 in turbulence along the domain as their residence time is short in comparison to the large-eddy turnover
 452 time of the flow.

453 The turbulent velocity fluctuations are responsible for enhancing the mixing of thermal energy within
 454 the radiated domain as the fluid-particle mixture is advected through it and exposed to radiation. The fluid
 455 is transparent to radiation, and consequently the radiative energy is only absorbed by particles and locally
 456 deposited to their surrounding fluid. However, the turbulent eddies efficiently convect high-temperature
 457 fluid volumes away from particle clusters and toward regions where the fluid is at lower temperatures. This
 458 stretching and straining experienced by the temperature field generates engulfing processes that maximize
 459 the transfer area between hot and cold regions, and where molecular diffusivity becomes more effective. As a
 460 result of the dissipative nature of turbulent flows, the velocity fluctuations slightly decay along the streamwise
 461 direction in the radiated domain since the turbulent forcing is only activated in the HIT section. In addition,
 462 the density of the fluid reduces by decrements of order unity resulting in smaller flow inertia with respect
 463 to the viscous forces. Nonetheless, the ratio of turbulence decay is much smaller than unity, and it does not
 464 have a significant impact on the turbulence levels of the flow. This third kinematic scale, thus, is largely
 465 related to the time-averaged volumetric increment of fluid temperature depicted in Figure 5 for I (a) and
 466 II (b). The remarkable resemblance between the distributions of normalized increments of fluid streamwise
 467 velocity, Figure 3, and temperature, Figure 5, is a direct consequence of momentum conservation. In detail,
 468 density changes are proportional to temperature variations through the equation of state, and therefore the
 469 conservation of momentum imposes that a reduction in density has to be compensated with a corresponding
 470 increment in velocity. An additional observation is that incrementing the number of particles by an order
 471 of magnitude does not result in a similar ratio of fluid temperature increase; instead of being of order $10\times$,

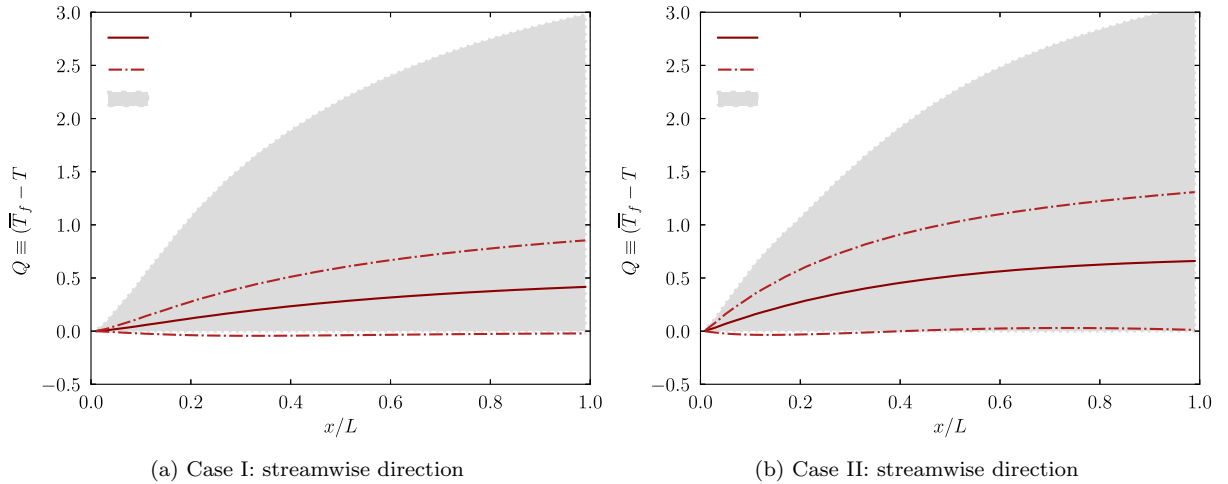


(a) Case I: slab of thickness $\Delta x/\eta = 10$ at inlet

(b) Case I: slab of thickness $\Delta x/\eta = 10$ at outlet

Figure 4: Particles RDF at inlet (a) and outlet (b) of the radiated domain for I. Solid lines correspond to the mean of the distributions, dashed lines indicate one standard deviation, and filled regions show the envelope of all samples.

472 the increment is $\sim 1.5\times$ from I to II. This feature notably highlights the quasi-saturation of the thermal
 473 transfer mechanisms in the system with respect to the number of particles.



(a) Case I: streamwise direction

(b) Case II: streamwise direction

Figure 5: Distribution of normalized temperature increment along the streamwise direction for I (a) and II (b). Solid lines correspond to the mean of the distributions, dashed lines indicate one standard deviation, and filled regions show the envelope of all samples.

474 5.2. Data-driven inference of principal π groups

475 Focusing on the normalized increment of fluid temperature $Q \equiv (\bar{T}_f - T_0)/T_0$, the data-driven polynomial
 476 ridge approximation strategy described in Section 3 is utilized to infer principal dimensionless groups from
 477 the data collected. This methodology requires one to approximate Q by a ridge function with a multivariate
 478 polynomial g of dimension n_p and total degree d in the form $Q \approx g(\mathbf{V}^\top \mathbf{x})$, where \mathbf{x} are the log-transformed
 479 inputs. By construction, n_p imposes the number of subspace dimensions (equivalent to dimensionless groups)

	Lower	Upper	M	L	T	H
<u>Case I:</u>						
$x/L = 0.0$	-0.21	+0.22	+0.25	+0.12	-0.62	+0.07
$x/L = 0.5$	-0.55	+0.08	+0.07	-0.01	-0.02	-0.03
$x/L = 1.0$	-0.45	+0.14	+0.04	-0.06	-0.22	+0.12
<u>Case II:</u>						
$x/L = 0.0$	-0.06	+0.53	+0.43	+0.55	-0.30	-0.19
$x/L = 0.5$	-0.31	+0.76	+0.37	-0.36	-0.55	-0.85
$x/L = 1.0$	-0.35	+0.81	+0.29	-0.16	-0.62	-0.73

Table 4: Subspace angle bootstrap 95% confidence intervals of $Q \equiv (\bar{T}_f - T_0)/T_0$ at different streamwise stations for I and II. Results are shown for the first subspace of the polynomial ridge function approximation. The confidence intervals include zero, which indicates that the estimated active subspace is compatible with the π subspace.

480 to be inferred, whereas d determines the degrees of freedom (polynomial order) available to fit the data along
481 each dimension.

482 The adequate n_p and d values are not known *a priori*. In consequence, a study based on the coefficient
483 of determination (CoD) is carried out to obtain suitable values for these two parameters as a first step of
484 the methodology. The CoD, typically denoted as R^2 , provides a measure of how well observed outcomes
485 are replicated by a model relative to the proportion of total variation of outcomes explained by it. Given
486 a dataset of $n = 128$ values y_1, \dots, y_n , each associated with a fitted, or modeled/predicted, value f_1, \dots, f_n
487 from which a residual $e_i = y_i - f_i$ can be computed, the mathematical definition of R^2 is written as

$$R^2 \equiv 1 - \frac{SS_{res}}{SS_{tot}}, \quad (25)$$

488 where $SS_{res} = \sum_{i=1}^n (y_i - f_i)^2 = \sum_{i=1}^n e_i^2$ is the residual sum of squares, and $SS_{tot} = \sum_{i=1}^n (y_i - \bar{y})^2$ is
489 the total sum of squares (proportional to the variance of the data) with $\bar{y} = n^{-1} \sum_{i=1}^n y_i$ the mean of the
490 observed data [64].

491 Following the definition introduced above, the R^2 analysis is summarized in Figure 6(a,b) by considering
492 Q at the outlet of I and II. The subspace dimensionality of Q slightly increases along the streamwise
493 direction as more radiative energy is absorbed by the system as shown in Figure 6(c,d). Thus, selecting
494 n_p and d for the data at the outlet will provide a polynomial model with enough dimensions and fitting
495 coefficients to be safely applied to infer dimensionless groups at different stations in the domain. The set of
496 subspace dimensions and polynomial degree combinations is constrained by the amount of data available.
497 Particularly, as shown in Figure 6, the maximum number of subspace dimensions is limited to 6, and the
498 highest polynomial degree is restricted to 4. The cross-validation is performed by splitting the data into 8
499 groups of same size, and the results are represented by means of boxplots [65]. As depicted in the figure,
500 restricting the polynomial g to 1 dimension is not sufficient for approximating the data, especially for II,
501 for which R^2 presents large variability skewed toward small values. In contrast, considering 3 dimensions
502 complicates the analysis, while it does not significantly increase R^2 with respect to $n_p = 2$. Therefore, the
503 pragmatic number of subspace dimensions for I and II is 2, constructed by utilizing polynomial degrees equal
504 to 3 and 4, respectively. This selection of polynomials results in R^2 values presenting small variability and
505 close to 1. In addition, these pragmatic configurations satisfy the subspace alignment criterion described in
506 Section 3.4 for different stations along the streamwise direction of the radiated domain as summarized in
507 Table 4; viz. since the bootstrap 95% confidence intervals contain the zero value, the estimated subspaces
508 are compatible with the corresponding π subspace, and the inferred π groups can be understood to be
509 approximately dimensionless at the chosen confidence level.

The projection weights \mathbf{V} of the polynomial ridge approximation for the two subspace dimensions of I
and II at the outlet of the radiated domain are provided in Table 5. As introduced in Section 3, weights
 \mathbf{v}_1 and \mathbf{v}_2 correspond, respectively, to the exponents of the input parameters composing each of the two
principal dimensionless groups, π_1 and π_2 , approximated by the polynomial ridge function. The labeling of
these two groups has been arranged such that π_1 is the subspace most aligned with the principal direction

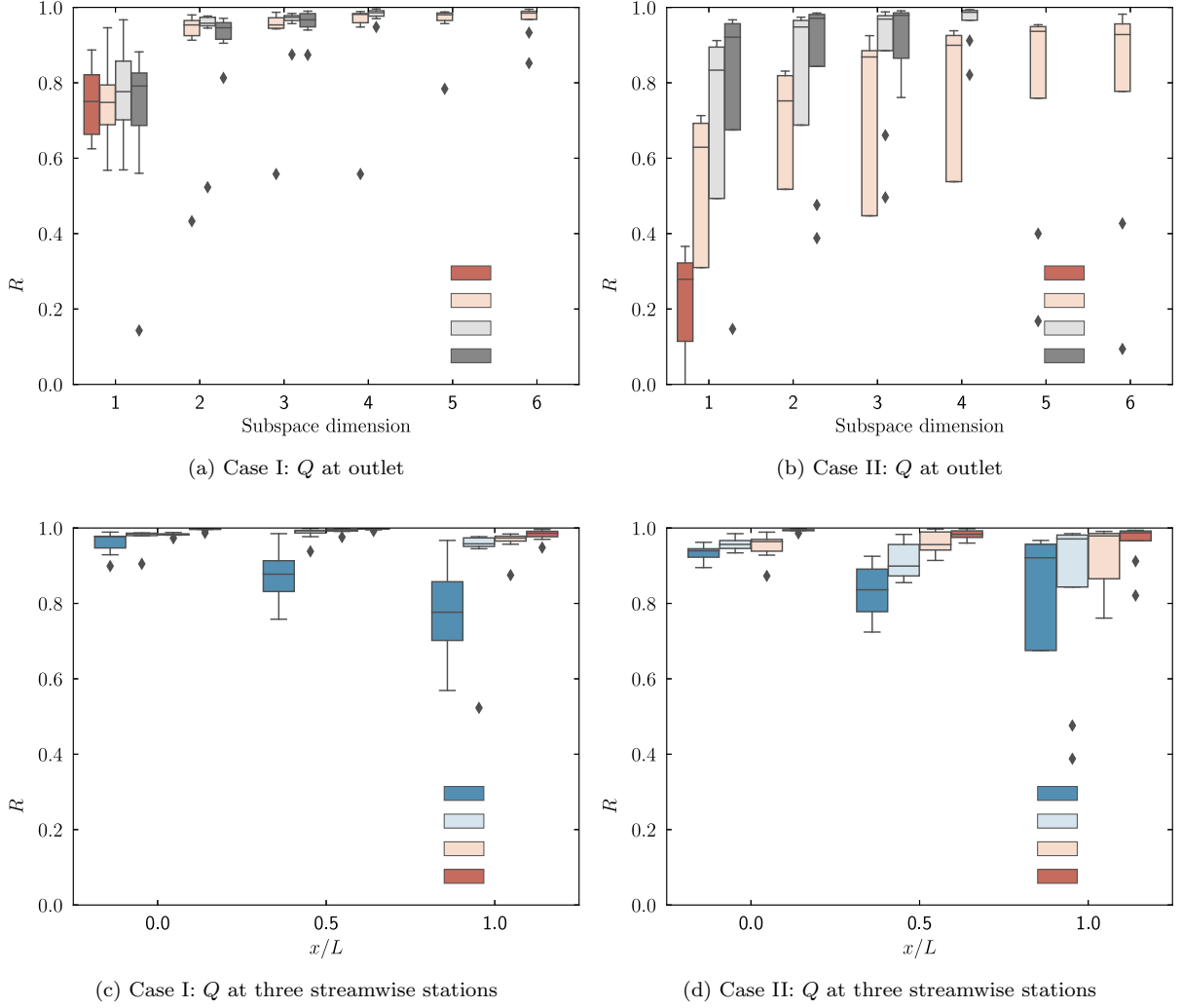


Figure 6: Coefficient of determination, R^2 , results of different subspace dimension and post-projection polynomial-fit order models for $Q \equiv (\bar{T}_f - T_0)/T_0$ at the outlet (a,b) and at three stations along the streamwise direction (c,d) for I (a,c) and II (b,d). The color scheme indicates the polynomial order (a,b) / subspace dimension (c,d) of the model. Boxplots display the minimum (small horizontal lines at Q1-1.5×IQR), maximum (small horizontal lines at Q3+1.5×IQR), whiskers (vertical lines), interquartile range (colored boxes spanning IQR=Q3-Q1), median (large horizontal lines), and outliers (diamonds) of the distributions. In panel d, due to the finite number of data points available, the polynomial degree is reduced to $d = 3$ when the subspace dimension is $n_p = 4$.

obtained from approximating the data with a 1-D polynomial ridge function. The values in the table are notably similar for I and II. This result indicates that the two cases investigated exhibit analogous behavior in terms of important dimensionless groups, and consequently the analysis below discusses them together by considering I. The R^2 results depicted in Figure 6 show that the first subspace dimension accounts for almost 80% of the variation in the data, and reaches values close to 100% when considering two dimensions. Focusing on the first subspace dimension, the data-driven inferred expression for the dimensionless group π_1 for $Q \equiv (\bar{T}_f - T_0)/T_0$ at the outlet of the radiated section is given by

$$\begin{aligned} \pi_1 = & W^{-0.510} \times L^{0.612} \times T_0^{-0.414} \times U_0^{-0.174} \times k_{\infty,f}^{-0.002} \times \rho_{f,0}^{-0.104} \times \mu_f^{0.001} \times \lambda_f^{-0.010} \\ & \times C_{P,f}^{-0.161} \times h^{0.013} \times N_{p,0}^{0.045} \times \rho_p^{-0.146} \times d_p^{0.002} \times C_{v,p}^{-0.095} \times \epsilon_p^{0.210} \times I_0^{0.224}. \end{aligned} \quad (26)$$

	W	L	T_0	U_0	$k_{\infty,f}$	$\rho_{f,0}$	μ_f	λ_f	$C_{P,f}$	h	$N_{p,0}$	ρ_p	d_p	$C_{v,p}$	ϵ_p	I_0
<u>Case I:</u>																
π_1	-0.510	0.612	-0.414	-0.174	-0.002	-0.104	0.001	-0.010	-0.161	0.013	0.045	-0.146	0.002	-0.095	0.210	0.224
π_2	-0.084	-0.491	-0.422	-0.069	0.027	-0.097	-0.074	0.053	-0.076	0.007	0.478	0.113	0.535	-0.032	0.084	0.101
<u>Case II:</u>																
π_1	-0.529	0.589	-0.418	-0.176	-0.003	-0.103	0.000	-0.007	-0.158	0.014	0.073	-0.141	0.011	-0.094	0.205	0.233
π_2	-0.109	-0.524	-0.374	-0.070	0.027	-0.114	-0.065	0.042	-0.102	0.004	0.444	0.119	0.563	-0.018	0.088	0.059

Table 5: Projection weights \mathbf{V} of the polynomial ridge approximation for I (top) and II (bottom) corresponding to the first (π_1) and second (π_2) subspace dimensions for $Q \equiv (\bar{T}_f - T_0)/T_0$ at the outlet of the radiated domain.

Analogously, the inferred definition for π_2 is

$$\pi_2 = W^{-0.084} \times L^{-0.491} \times T_0^{-0.422} \times U_0^{-0.069} \times k_{\infty,f}^{0.027} \times \rho_{f,0}^{-0.097} \times \mu_f^{-0.074} \times \lambda_f^{0.053} \times C_{P,f}^{-0.076} \times h^{0.007} \times N_{p,0}^{0.478} \times \rho_p^{0.113} \times d_p^{0.535} \times C_{v,p}^{-0.032} \times \epsilon_p^{0.084} \times I_0^{0.101}. \quad (27)$$

510 These expressions provide a quantitative decomposition of the principal π groups as a function of the
511 independent (input) parameters of the problem. A more insightful, and easier to interpret, decomposition
512 in terms of “standard” fluid mechanics dimensionless numbers will be discussed in the next subsection.

513 The input-to-output response of Q at the outlet of the radiated domain as a function of the π groups
514 inferred by the ridge function polynomial is depicted in Figure 7. The fit obtained by the first subspace
515 dimension shown in Figure 7(a) reveals that Q increases monotonically with π_1 , and presents exponential
516 growth for $\pi_1 > 1$. In addition, the 2-D summary plot depicted in Figure 7(b) qualitatively indicates that Q
517 generally increases also with π_2 . However, as shown by the plot, the importance of this second dimensionless
518 group is significantly small with respect to π_1 as most of the variation in the data (color gradient) is captured
519 by the latter.

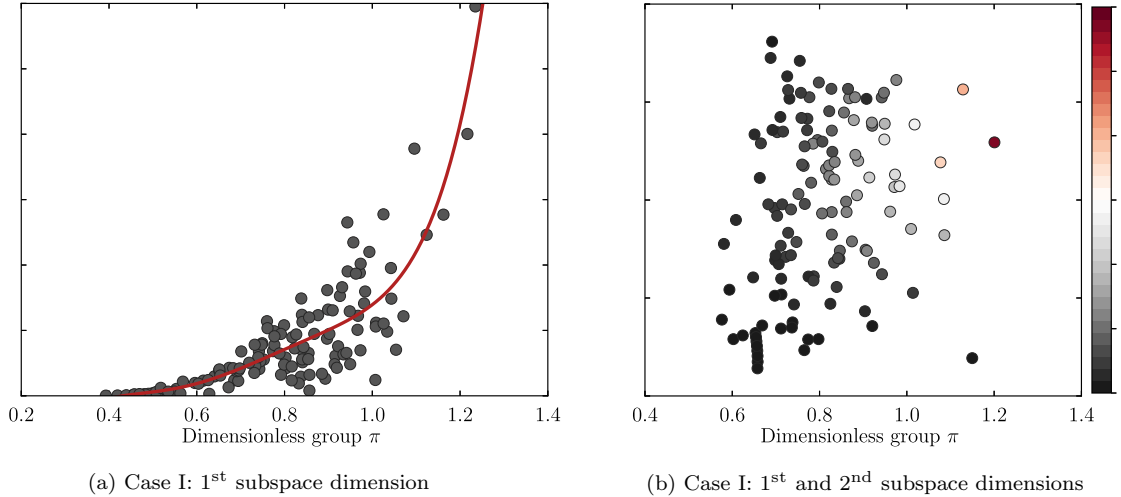


Figure 7: Summary plots of the 2-D ridge function fit versus the inferred dimensionless groups π_1 (a) and (b) $\pi_1 - \pi_2$ with a third-order degree polynomial for $Q \equiv (\bar{T}_f - T_0)/T_0$ of I at the outlet.

520 5.3. Interpretation in terms of “standard” dimensionless numbers

As introduced in Section 1.2, the identification and characterization of important dimensionless groups can be notably enhanced by inspectional analysis of the scale-free equations describing the problem. The

data-driven methodology described in Section 3 is compatible with this form of dimensional analysis by allowing one to easily re-express the π groups as powers of “standard” dimensionless numbers (19) through a simple linear algebra transformation (18). As a basis for re-expression of the π groups, we consider widely recognized dimensionless numbers in fluid mechanics resulting from normalizing the equations introduced in Section 2. Replacing the dimensioned variables with their corresponding dimensionless counterparts (denoted by superscript \star) using the scalings

$$\begin{aligned}\mathbf{x} &= \lambda_T \mathbf{x}^\star, & t &= (\lambda_T/u_{rms}) t^\star, & \mathbf{u} &= u_{rms} \mathbf{u}^\star, \\ \rho &= \rho_{f,0} \rho^\star, & T &= T_0 T^\star, & P &= \rho_{f,0} u_{rms}^2 P^\star,\end{aligned}\quad (28)$$

with $\lambda_T = (200/3)^{1/4} \sqrt{W\mu_f / (\rho_{f,0} u_{rms})}$ the Taylor microscale of the flow, the following set of dimensionless equations of motion are obtained for the carrier phase

$$\frac{\partial \rho_f^\star}{\partial t^\star} + \nabla^\star \cdot (\rho_f^\star \mathbf{u}_f^\star) = 0, \quad (29)$$

$$\frac{\partial (\rho_f^\star \mathbf{u}_f^\star)}{\partial t^\star} + \nabla^\star \cdot (\rho_f^\star \mathbf{u}_f^\star \otimes \mathbf{u}_f^\star) = -\nabla^\star p^\star + \frac{1}{Re_\lambda} \nabla^\star \cdot \left[(\nabla^\star \mathbf{u}_f^\star + \nabla^\star \mathbf{u}_f^{\star T}) - \frac{2}{3} (\nabla^\star \cdot \mathbf{u}_f^\star) \mathbf{I} \right] + \mathbf{f}_{TWC}^\star, \quad (30)$$

$$\frac{1}{\gamma} \frac{\partial (\rho_f^\star T_f^\star)}{\partial t^\star} + \nabla^\star \cdot (\rho_f^\star T_f^\star \mathbf{u}_f^\star) = \frac{1}{Re_\lambda Pr} \nabla^{\star 2} T_f^\star + S_{TWC}^\star, \quad (31)$$

521 in combination with the nondimensional EoS $P_{th}^\star = \rho_f^\star T_f^\star / (\gamma Ma^2)$, and two-way coupling terms

$$\mathbf{f}_{TWC}^\star = \sqrt{15} \frac{MLR}{St_\eta N_{p,0}} \sum_p (\mathbf{v}_p^\star - \mathbf{u}_p^\star) \delta^\star(\mathbf{x}^\star - \mathbf{x}_p^\star), \quad S_{TWC}^\star = \frac{\sqrt{15}}{3} \frac{MLR Nu}{Pr St_\eta N_{p,0}} \sum_p (T_p^\star - T_f^\star) \delta^\star(\mathbf{x}^\star - \mathbf{x}_p^\star). \quad (32)$$

Similarly, the dimensionless conservation equations for the dispersed phase result in

$$\frac{d\mathbf{x}_p^\star}{dt^\star} = \mathbf{v}_p^\star, \quad (33)$$

$$\frac{d\mathbf{v}_p^\star}{dt^\star} = \sqrt{15} \frac{(\mathbf{u}_p^\star - \mathbf{v}_p^\star)}{St_\eta}, \quad (34)$$

$$\frac{dT_p^\star}{dt^\star} = \sqrt{\frac{200}{3}} \frac{Re_W \epsilon_p \mathcal{R}}{Re_\lambda^2} - \frac{\sqrt{15}}{3} \frac{Nu \gamma}{Pr St_\eta \chi} (T_p^\star - T_f^\star). \quad (35)$$

522 As indicated by Buckingham’s π theorem (10), $n_d = 16$ independent variables minus 4 base units equals $n_p =$
523 12 independent dimensionless groups, which are identified from normalizing the equations and boundary
524 conditions. Their definitions and physical interpretation are given in Table 6, where the relaxation time of
525 the flow based on the Kolmogorov scale is $\tau_\eta = \lambda_T / (\sqrt{15} u_{rms})$ and its associated length scale corresponds
526 to $\eta = u_{rms} \tau_\eta$. In addition, particles are assumed to be perfectly spherical with mass $m_p = \pi \rho_p d_p^3 / 6$.

Utilizing the set of dimensionless numbers listed in Table 6 as the transformation basis, the π_1 and π_2 dimensionless groups inferred from data in the previous subsection can be re-expressed as products of “standard” fluid mechanics groups with exponents given by the values shown in Table 7. Considering I as in the subsection above, the decomposition for the first dimensionless group corresponds to

$$\pi_1 = AR^{0.591} \times N_{p,0}^{0.062} \times Ma^{0.146} \times Pr^{0.036} \times Nu^{0.004} \times \chi^{0.154} \quad (36)$$

$$\begin{aligned}& \times Re_\lambda^{-0.297} \times MLR^{-0.017} \times St_\eta^{0.153} \times Re_W^{0.120} \times \epsilon_p^{0.210} \times \mathcal{R}^{0.278}, \\ & \approx \frac{AR^{0.6} \times \epsilon_p^{0.2} \times \mathcal{R}^{0.3}}{Re_\lambda^{0.3}} = \tilde{\pi}_1,\end{aligned}\quad (37)$$

Dimensionless number	Definition	Physical interpretation
<u>Kinematic groups:</u>		
Domain aspect ratio	$AR = L/W$	Length to width ratio of radiated domain
Number of particles	$N_{p,0} = n_{p,0}\lambda_T^3$	Initial number of particles in HIT domain
<u>Thermophysical groups:</u>		
Mach number	$Ma = u_{rms}/\sqrt{\gamma R_f T_0}$	Flow velocity to speed of sound ratio
Prandtl number	$Pr = C_{P,f}\mu_f/\lambda_f$	Momentum to thermal diffusivities ratio
Adiabatic index	$\gamma = C_{P,f}/C_{v,f}$	Isobaric to isochoric heat capacities ratio
Nusselt number	$Nu = hd_p/\lambda_f$	Convective to conductive heat transfer ratio
Particle-fluid heat capacities	$\chi = C_{v,p}/C_{v,f}$	Particle to fluid heat capacities ratio
<u>Hydrodynamic groups:</u>		
Taylor Reynolds number	$Re_\lambda = \rho_{f,0}u_{rms}\lambda_T/\mu_f$	Inertial (HIT) to viscous forces ratio
Mass loading ratio	$MLR = n_{p,0}m_p/\rho_{f,0}$	Particles to fluid masses ratio
Kolmogorov Stokes number	$St_\eta = \tau_p/\tau_\eta$	Particle to fluid relaxation times ratio
Bulk Reynolds number	$Re_W = \rho_{f,0}U_0W/\mu_f$	Inertial (bulk) to viscous forces ratio
<u>Radiometric groups:</u>		
Particles absorption coefficient	ϵ_p	Absorbed to incident radiation ratio
Radiation transfer number	$\mathcal{R} = \lambda_T\pi d_p^2 I_0/(4T_0U_0m_pC_{v,p})$	Source rate to convective transport ratio

Table 6: List of “standard” fluid mechanics dimensionless numbers. The adiabatic index is assumed constant in this work (diatomic ideal gases: $\gamma = 1.4$), and therefore is not considered an independent dimensionless number. The radiation transfer number \mathcal{R} is similar to the Damköhler number in chemically reacting flows.

	AR	$N_{p,0}$	Ma	Pr	Nu	χ	Re_λ	MLR	St_η	Re_W	ϵ_p	\mathcal{R}
<u>Case I:</u>												
π_1	0.591	0.062	0.146	0.036	0.004	0.154	-0.297	-0.017	0.153	0.120	0.210	0.278
π_2	-0.464	0.167	0.189	0.050	-0.062	0.074	-0.621	0.311	-0.071	0.136	0.084	0.169
<u>Case II:</u>												
π_1	0.577	0.069	0.145	0.038	-0.002	0.155	-0.308	0.004	0.135	0.122	0.205	0.281
π_2	-0.495	0.102	0.235	0.027	-0.047	0.063	-0.580	0.342	-0.128	0.098	0.088	0.132

Table 7: Exponents of the “standard” fluid mechanics dimensionless numbers for I (top) and II (bottom) composing the first (π_1) and second (π_2) subspace dimensions for $Q \equiv (\bar{T}_f - T_0)/T_0$ at the outlet of the radiated domain.

and for the second group is given by

$$\pi_2 = AR^{-0.464} \times N_{p,0}^{0.167} \times Ma^{0.189} \times Pr^{0.050} \times Nu^{-0.062} \times \chi^{0.074} \quad (38)$$

$$\times Re_\lambda^{-0.621} \times MLR^{0.311} \times St_\eta^{-0.071} \times Re_W^{0.136} \times \epsilon_p^{0.084} \times \mathcal{R}^{0.169},$$

$$\approx \frac{MLR^{0.3}}{AR^{0.5} Re_\lambda^{0.6}} = \tilde{\pi}_2, \quad (39)$$

527 where a threshold of $|w_{ij}| \geq 0.2$ has been utilized to obtain the approximated $\tilde{\pi}$ groups; different threshold
528 values have been tested, concluding that 0.2 provides a good balance between accuracy and simplification.

529 The structure of the two dimensionless groups rounded in Eqs. (37) and (39) indicates that AR and Re_λ
530 play a major role in dictating the system’s response in terms of $Q \equiv (\bar{T}_f - T_0)/T_0$ as they contribute to both
531 $\tilde{\pi}_1$ and $\tilde{\pi}_2$. The first dimensionless group, $\tilde{\pi}_1$, also involves the radiometric dimensionless numbers ϵ_p and
532 \mathcal{R} , and consequently is largely connected to the transfer of radiative energy encompassing the absorption by
533 particles and the subsequent deposition to the carrier phase as the mixture is advected through the radiated
534 domain. Instead, $\tilde{\pi}_2$ includes MLR , and therefore is related to the number of particles with respect to the
535 fluid phase. For example, the composition of $\tilde{\pi}_1$ indicates that augmenting AR , ϵ_p and/or \mathcal{R} results in an
536 increase of Q , while enlarging Re_λ translates into decreasing Q .

537 Focusing on $\tilde{\pi}_1$, which accounts for most of the variation in Q , the larger the length L of the radiated
538 domain with respect to W , the more energy is absorbed by the system, resulting in higher fluid temperatures

at the outlet. However, AR may be imposed, or constrained, in practical engineering problems. In that case, ϵ_p , \mathcal{R} and Re_λ become the most sensitive parameters for controlling the thermal response of irradiated particle-laden turbulence systems. Inspecting the position of these dimensionless numbers in the scale-free equations (29)-(35), it can be seen that: (i) Re_λ is found in the denominators of the terms multiplying the diffusion fluxes in the momentum and energy equations of the carrier phase, (30) and (31), and the radiation absorption by particles in the temperature equation of the dispersed phase, (35), implying that small Re_λ values result in large diffusion fluxes in the carrier phase, which contribute to the mixing of thermal energy at the small scales, in addition to large quantities of radiation absorbed by the particles; (ii) ϵ_p and \mathcal{R} are only encountered in the numerator of the first term on the right-hand-side of (35), which in combination with Re_λ in the denominator, indicates that larger absorption and deposition rates of radiative thermal energy together with lower levels of turbulence translates into larger fluid temperature values in the system.

Connecting these final observations with the thermal-fluid characterization of the system discussed in Section 5.1, the present study suggests that the bulk velocity, U_0 (found in the denominator of \mathcal{R}), and the turbulent velocity fluctuations, u_{rms} (part of the numerator of Re_λ), are the most sensitive kinematic scales for determining the total amount of energy absorbed in irradiated particle-laden turbulence, whereas the slip velocity between the two phases, $u_p - v_p$ (directly proportional to St_η), plays a secondary role with a similar level of importance as χ and Re_W . From a control-volume (integral) analysis perspective, this result indicates that the radiative energy volumetrically transferred to the fluid does not depend significantly on the local deposition through the particles, but on the ratio of radiative source to convective transport and the thermal mixing rate of the flow. However, if the relevant QoI was, for instance, the spatial distribution or temporal fluctuation of T_f , the relative importance of the “standard” dimensionless numbers composing the principal π groups could be largely dependent on the slip velocity between phases through St_η . A related study has been performed by Pouransari & Mani [17]. In their work, the effects of varying St_η (keeping the other dimensionless numbers fixed) on the heat transfer statistics in a similar problem configuration are comprehensively analyzed. For example, they found that changes in the preferential concentration of particles can modify the effective heat transfer up to 25%. Instead, this work demonstrates in Figure 5 that ratios of variation of $\sim 5\times$ can be achieved if considering a larger number of input parameters as independent variables of the system.

6. Summary, conclusions and future work

Multiphysics flow problems, such as irradiated particle-laden turbulence, (typically) involve the analysis of complex high-dimensional parameter spaces. Their study can be systematically approached by considering important dimensionless groups characterizing the underlying physics phenomena, which, in addition to reducing the dimensionality of the system, provide great support for the inference of similarity laws and a basis for out-of-scale modeling. However, classical dimensional analysis techniques present two main shortfalls as the set of scale-free groups are not unique, and there is no general methodology for quantifying their relative importance and physically interpreting the results. This work, therefore, has proposed a data-driven methodology aimed to address these deficiencies by augmenting Buckingham’s π theorem with ideas developed in the field of dimension reduction tailored to the study of large-scale, complex turbulent flow applications.

A concise physics analysis of the irradiated particle-laden turbulence system studied has been performed to characterize the thermo-fluid mechanisms encountered. Three main kinematic scales have been identified corresponding to the bulk velocity U_0 , the slip velocity of particles $u_p - v_p$, and the turbulent velocity fluctuations u_{rms} , which are mainly responsible for the residence time of the fluid-particle mixture, the spatial distribution of particles, and the thermal mixing within the fluid, respectively. The small variation of the particles’ radial distribution functions along the streamwise direction has revealed that the residence time of the fluid-particle mixture is short in comparison to the large-eddy turnover time of the flow, but larger than the thermal response time of the system. Consequently, the computational setup utilized to infer important dimensionless groups in irradiated particle-laden turbulence is appropriate for its designed purpose. The comparison between the two cases considered indicates that the thermal response of the

588 system studied is quasi-saturated with regards to the number of particles; viz. incrementing the number of
589 particles by an order of magnitude results in an increase of fluid temperature of $\sim 1.5\times$.

590 The data-driven methodology presented has been utilized to infer important dimensionless groups of the
591 problem. Two important dimensionless groups have been identified by approximating the active subspaces
592 of the data with polynomial ridge functions. Their decomposition in terms of “standard” fluid mechanics
593 dimensionless numbers indicate that the mass loading ratio MLR and, especially, the aspect ratio AR , the
594 Taylor Reynolds number Re_λ , the particle absorption coefficient ϵ_p , and the radiation transfer number
595 \mathcal{R} contribute the most to the variation of the system’s thermal response in terms of fluid temperature
596 increment at the outlet of the radiated domain. The CoD achieved by considering the first dimensionless
597 group is approximately 80%, and increases to practically 100% when considering the two groups together.
598 Its analysis, combined with the scale-free conservation equations, shows that, rather than the distribution
599 of particles and thermophysical properties of the two (carrier and dispersed) phases, the most important
600 mechanisms for controlling the temperature of the fluid in the system are the absorption of radiation by
601 particles, the radiative energy deposition rate, and the turbulent flow mixing. The results are similar for
602 the two cases considered, which differ by an order of magnitude in the number of particles, and therefore
603 suggest that they may be generalizable to wider ranges of dispersed phase loading.

604 Future work will focus on expanding the data-driven methodology to generate simplified decompositions
605 of the dimensionless groups inferred by means of L1-regularization (Lasso regression) approaches. In addi-
606 tion, wider ranges of dispersed phase loading will be analyzed to further corroborate the scientific findings
607 described in this work, and to carry out studies for the engineering optimization of radiative energy transfer
608 in particle-laden turbulent flows.

609 Acknowledgments

610 This work was funded by the United States Department of Energy’s National Nuclear Security Ad-
611 ministration under the Predictive Science Academic Alliance Program II at Stanford University, Grant
612 DE-NA-0002373. L.J. acknowledges funding by the Beatriz Galindo Program (Distinguished Researcher,
613 BGP18/00026) of the Ministerio de Ciencia, Innovación y Universidades, Spain.

614 An award of computer time was provided by the ASCR Leadership Computing Challenge program. This
615 research used resources of the Argonne Leadership Computing Facility, which is a Department of Energy’s
616 Office of Science User Facility supported under contract DE-AC02-06CH11357. This research also used
617 resources of the Oak Ridge Leadership Computing Facility, which is a Department of Energy’s Office of
618 Science User Facility supported under contract DE-AC05-00OR22725.

619 References

- 620 [1] F. Veron, Ocean spray, *Annu. Rev. Fluid Mech.* 47 (2015) 507–538.
621 [2] R. A. Shaw, Particle-turbulence interactions in atmospheric clouds, *Annu. Rev. Fluid Mech.* 35 (2003) 183–227.
622 [3] S. R. Tieszen, On the fluid mechanics of fires, *Annu. Rev. Fluid Mech.* 33 (2001) 67–92.
623 [4] J. C. Lasheras, E. J. Hopfinger, Liquid jet instability and atomization in a coaxial gas stream, *Annu. Rev. Fluid Mech.*
624 32 (2000) 275–308.
625 [5] M. S. Dodd, L. Jofre, Small-scale flow topologies in decaying isotropic turbulence laden with finite-size droplets, *Phys.*
626 *Rev. Fluids* 4 (2019) 064303.
627 [6] V. Raman, R. O. Fox, Modeling of fine-particle formation in turbulent flames, *Annu. Rev. Fluid Mech.* 48 (2016) 159–190.
628 [7] C. K. Ho, Advances in central receivers for concentrating solar applications, *Sol. Energy* 152 (2017) 38–56.
629 [8] S. Balachandar, J. K. Eaton, Turbulent dispersed multiphase flow, *Annu. Rev. Fluid Mech.* 42 (2010) 111–133.
630 [9] M. Caporaloni, F. Tampieri, F. Trombetti, O. Vittori, Transfer of particles in nonisotropic air turbulence, *J. Atmos. Sci.*
631 32 (1975) 565–568.
632 [10] K. D. Squires, J. K. Eaton, Preferential concentration of particles by turbulence, *Phys. Fluids A* 3 (1991) 1169–1178.
633 [11] L. Jofre, G. Geraci, H. R. Fairbanks, A. Doostan, G. Iaccarino, Multi-fidelity uncertainty quantification of irradiated
634 particle-laden turbulence, *CTR Annu. Res. Briefs* (2017) 21–34.
635 [12] H. R. Fairbanks, L. Jofre, G. Geraci, G. Iaccarino, A. Doostan, Bi-fidelity approximation for uncertainty quantification
636 and sensitivity analysis of irradiated particle-laden turbulence, *J. Comput. Phys.* 402 (2020) 108996.
637 [13] A. M. Dunton, L. Jofre, A. Doostan, G. Iaccarino, Pass-efficient methods for compression of high-dimensional turbulent
638 flow data, *CTR Annu. Res. Briefs* (2017) 313–325.

- 639 [14] L. Jofre, Z. R. del Rosario, G. Iaccarino, Dimension reduction of thermo-fluid mechanisms in irradiated particle-laden
640 turbulence, *CTR Annu. Res. Briefs* (2019) 1–14.
- 641 [15] R. Zamansky, F. Coletti, M. Massot, A. Mani, Radiation induces turbulence in particle-laden fluids, *Phys. Fluids* 26
642 (2014) 071701.
- 643 [16] A. Frankel, H. Pouransari, F. Coletti, A. Mani, Settling of heated particles in homogeneous turbulence, *J. Fluid Mech.*
644 792 (2016) 869–893.
- 645 [17] H. Pouransari, A. Mani, Effects of preferential concentration on heat transfer in particle-based solar receivers, *J. Sol.*
646 *Energy Eng.* 139 (2017) 021008.
- 647 [18] M. Rahmani, G. Geraci, G. Iaccarino, A. Mani, Effects of particle polydispersity on radiative heat transfer in particle-laden
648 turbulent flows, *Int. J. Multiph. Flow* 104 (2018) 42–59.
- 649 [19] B. J. Cantwell, *Introduction to Symmetry Analysis*, Cambridge University Press, 2002.
- 650 [20] V. Simon, B. Weigand, H. Gomma, *Dimensional Analysis for Engineers*, Springer, 2017.
- 651 [21] E. O. Macagno, Historico-critical review of dimensional analysis, *J. Franklin Inst.* 291 (1971) 391–402.
- 652 [22] E. Buckingham, On physically similar systems; illustrations of the use of dimensional equations, *Phys. Rev.* 4 (1914)
653 345–376.
- 654 [23] P. W. Bridgman, *Dimensional Analysis*, Yale University Press, 1922.
- 655 [24] J. D. Anderson, *Fundamentals of Aerodynamics*, McGraw-Hill, 1984.
- 656 [25] N. Peters, *Turbulent Combustion*, Cambridge University Press, 2000.
- 657 [26] M. F. Modest, *Radiative Heat Transfer*, Elsevier, 1993.
- 658 [27] R. Kurth, *Dimensional Analysis and Group Theory in Astrophysics*, Elsevier, 1972.
- 659 [28] R. M. Brach, *Mechanical Impact Dynamics: Rigid Body Collisions*, John Wiley & Sons, 1991.
- 660 [29] J. Worstell, *Dimensional Analysis: Practical Guides in Chemical Engineering*, Elsevier, 2014.
- 661 [30] W. R. Stahl, Dimensional analysis in mathematical biology. I General discussion, *Bull. Math. Biol.* 28 (1961) 355–376.
- 662 [31] M. Pohl, A. Ristig, W. Schachermayer, L. Tangpi, The amazing power of dimensional analysis: quantifying market impact,
663 *Market Microstructure and Liquidity* 3 (2017) 1850004.
- 664 [32] Z. del Rosario, M. Lee, G. Iaccarino, Lurking variable detection via dimensional analysis, *SIAM-ASA J. Uncertain. Quan.*
665 7 (2019) 232–259.
- 666 [33] P. G. Constantine, Z. del Rosario, G. Iaccarino, Data-driven dimensional analysis: algorithms for unique and relevant
667 dimensionless groups, arXiv preprint arXiv:1708.04303 (2017).
- 668 [34] A. Pinkus, *Ridge Functions*, Cambridge University Press, Cambridge, 2015.
- 669 [35] J. M. Hokanson, P. G. Constantine, Data-driven polynomial ridge approximation using variable projection, *SIAM J. Sci.*
670 *Comput.* 40 (2018) A1566–A1589.
- 671 [36] P. G. Constantine, *Active Subspaces: Emerging Ideas for Dimension Reduction in Parameter Studies*, SIAM Philadelphia,
672 2015.
- 673 [37] S. Subramaniam, Lagrangian-Eulerian methods for multiphase flows, *Prog. Energy Combust. Sci.* 39 (2013) 215–245.
- 674 [38] M. R. Maxey, J. J. Riley, Equation of motion for a small rigid sphere in a nonuniform flow, *Phys. Fluids* 26 (1983)
675 883–889.
- 676 [39] M. Esmaily, L. Jofre, A. Mani, G. Iaccarino, A scalable geometric multigrid solver for nonsymmetric elliptic systems with
677 application to variable-density flows, *J. Comput. Phys.* 357 (2018) 142–158.
- 678 [40] Soleil-X: turbulence/particle/radiation solver written in the Regent language for execution with the Legion runtime,
679 <https://github.com/stanfordhpccenter/soleil-x>, 2014-2019.
- 680 [41] H. Torres, M. Papadakis, L. Jofre, W. Lee, A. Aiken, G. Iaccarino, Soleil-X: turbulence, particles, and radiation in the
681 Regent programming language, in: *SC19 IEEE/ACM Parallel Applications Workshop, Alternatives To MPI (PAW-ATM)*,
682 pp. 1–4.
- 683 [42] Exascale Computing Engineering Center. Predictive Science Academic Alliance Program (PSAAP) II, Stanford University,
684 <http://exascale.stanford.edu>, 2014-2019.
- 685 [43] G. I. Park, M. Bassenne, J. Urzay, P. Moin, A simple dynamic subgrid-scale model for LES of particle-laden turbulence,
686 *Phys. Rev. Fluids* 2 (2017) 044301.
- 687 [44] L. Jofre, S. P. Domino, G. Iaccarino, A framework for characterizing structural uncertainty in large-eddy simulation
688 closures, *Flow Turbul. Combust.* 100 (2018) 341–363.
- 689 [45] `pybuck`: dimensional analysis in Python, <https://github.com/zdelrosario/pybuck>, 2019.
- 690 [46] G. I. Barenblatt, *Scaling, self-similarity, and intermediate asymptotics: dimensional analysis and intermediate asymptotics*,
691 Cambridge University Press, 1996.
- 692 [47] O. Reynolds, An experimental investigation of the circumstances which determine whether the motion of water shall be
693 direct or sinuous, and of the law of resistance in parallel channels, *Proc. R. Soc. Lond.* 35 (1883) 84–99.
- 694 [48] J. D. Jackson, L. B. Okun, Historical roots of gauge invariance, *Rev. Mod. Phys.* 73 (2001) 663.
- 695 [49] T. M. Russi, Uncertainty quantification with experimental data and complex system models, Ph.D. thesis, UC Berkeley,
696 2010.
- 697 [50] M. R. Lee, Modified active subspaces using the average of gradients, *SIAM-ASA J. Uncertain. Quan.* 7 (2019) 53–66.
- 698 [51] R. D. Cook, *Regression Graphics: Ideas for Studying Regressions Through Graphics*, John Wiley & Sons, 2009.
- 699 [52] J. Nikuradse, *Laws of Flow in Rough Pipes*, National Advisory Committee for Aeronautics, 1950.
- 700 [53] B. L. Joiner, Lurking variables: some examples, *Am. Stat.* 35 (1981) 227–233.
- 701 [54] S. Shvartsman, Personal communication, 2016.
- 702 [55] G. H. Golub, C. F. Van Loan, *Matrix Computations*, volume 4, JHU Press, 2013.
- 703 [56] B. Efron, R. J. Tibshirani, *An Introduction to the Bootstrap*, CRC Press, 1994.

- 704 [57] M. Bassenne, J. Urzay, G. I. Park, P. Moin, Constant-energetics physical-space forcing methods for improved convergence
705 to homogeneous-isotropic turbulence with applications to particle-laden flows, *Phys. Fluids* 28 (2016) 035114.
- 706 [58] B. E. Poling, J. M. Prausnitz, J. P. O'Connell, *The Properties of Gases and Liquids*, McGraw-Hill, 2001.
- 707 [59] S. B. Pope, *Turbulent Flows*, Cambridge University Press, 2000.
- 708 [60] A. B. Owen, A randomized Halton algorithm in R, arXiv preprint arXiv:1706.02808 (2017).
- 709 [61] J. Urzay, M. Bassenne, G. I. Park, P. Moin, Characteristic regimes of subgrid-scale coupling in LES of particle-laden
710 turbulent flows, *CTR Annu. Res. Briefs* (2014) 3–13.
- 711 [62] B. Ray, L. R. Collins, Preferential concentration and relative velocity statistics of inertial particles in Navier-Stokes
712 turbulence with and without filtering, *J. Fluid Mech.* 680 (2011) 488–510.
- 713 [63] G. Jin, G.-W. He, L.-P. Wang, Large-eddy simulation of turbulent collision of heavy particles in isotropic turbulence,
714 *Phys. Fluids* 22 (2010) 055106.
- 715 [64] S. Weisberg, *Applied Linear Regression*, John Wiley & Sons, 2005.
- 716 [65] J. W. Tukey, *Exploratory Data Analysis*, Addison-Wesley Publishing Company, 1977.